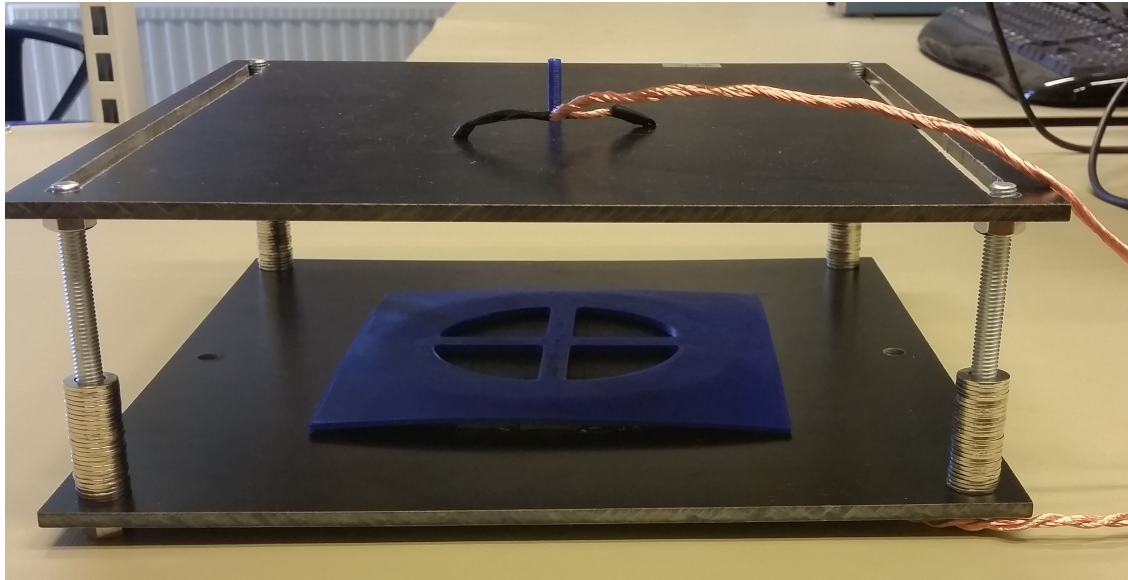




**CHALMERS**  
UNIVERSITY OF TECHNOLOGY

---



# Inductive charging for a self-balancing robot

Design and development of prototype

Master's thesis in Electric Power Engineering

FREDRIK CARLSSON  
OLA BÅÅTH



# Inductive charging for a self-balancing robot

Design and development of prototype

FREDRIK CARLSSON  
OLA BÅÅTH



**CHALMERS**  
UNIVERSITY OF TECHNOLOGY

Department of Energy and Environment  
*Division of Electric Power Engineering*  
CHALMERS UNIVERSITY OF TECHNOLOGY  
Gothenburg, Sweden 2016

Inductive charging for a self-balancing robot  
Design and development of prototype  
FREDRIK CARLSSON  
OLA BÅÅTH

© FREDRIK CARLSSON  
OLA BÅÅTH, 2016.

Supervisor: Mikael Alatalo, Aros Electronics  
Examiner: Torbjörn Thiringer, Energy and Environment

Department of Energy and Environment  
Division of Electric Power Engineering  
Chalmers University of Technology  
SE-412 96 Gothenburg  
Telephone +46 31 772 1000

Cover: Test stand with transmitting and receiving power pads.

Typeset in L<sup>A</sup>T<sub>E</sub>X  
Gothenburg, Sweden 2016

Inductive charging for a self-balancing robot  
Design and development of prototype  
FREDRIK CARLSSON  
OLA BÅÅTH  
Department of Energy and Environment  
Chalmers University of Technology

## Abstract

In this master's thesis project an inductive power transfer (IPT) system is designed and developed. This IPT system should in the future be implemented in Aros Electronics self-balancing robot Glenn. The system can transfer 153  $W$  over a 3  $cm$  air gap with an efficiency of 84.5 %. Furthermore, the IPT system is able to transfer 100  $W$  with a misalignment between the power pads of 4  $cm$  as well as an increased air gap to 4  $cm$ . The IPT system has been designed by iterations between COMSOL simulations and circuit simulations in LT spice.

The power supply in the IPT system produces a 83  $kHz$  square-wave voltage. The system uses series-series capacitive compensation to achieve resonance on the transmitting and receiving circuits. With the series-series compensation the systems functions as a voltage source and the compensations is independent of load and the mutual inductance, making it a suitable choice for charging of batteries.

The transmitting and receiving coils are made of litz wire to decrease skin effect and proximity effect. The coils are placed on ferrite plates to increase the magnetic field and mutual inductance between the coils, resulting in two power pads.

Keywords: Inductive power transfer (IPT), power pad, litz wire, misalignment, air gap.



## Acknowledgements

First and foremost we would like to express our appreciation for our supervisor from Aros Electronics, Mikael Alatalo, for his technical support and guidance throughout this project. Furthermore, we would like to express our gratitude to our supervisor and examiner from Chalmers University of Technology, Torbjörn Thiringer, for all the meetings and insightful feedback. Also, we would like to thank Daniel Pehrman, PhD student from Chalmers, for rewarding discussions and guidance. Finally, we would like to thank Aros Electronics for the opportunity, as well as all the employees that has shared their knowledge with us and provided us with very useful support.

Fredrik Carlsson & Ola Bååth, Gothenburg, 06 2016



# Contents

<b>1</b>	<b>Introduction</b>	<b>1</b>
1.1	Background . . . . .	1
1.2	Previous work . . . . .	2
1.3	Purpose . . . . .	2
<b>2</b>	<b>Theory</b>	<b>3</b>
2.1	Inductive power transfer . . . . .	3
2.1.1	Mutual inductance and coupling factor . . . . .	3
2.1.2	Inductive power transfer model . . . . .	5
2.1.3	Misalignment between coils and change in air gap . . . . .	5
2.1.4	Resonant circuits . . . . .	6
2.2	DC to AC inverter . . . . .	8
2.2.1	Single phase full bridge inverter . . . . .	9
2.2.1.1	Conduction and switching losses . . . . .	10
2.3	AC to DC rectifier . . . . .	11
2.3.1	Single phase diode bridge rectifier . . . . .	11
2.3.1.1	Conduction losses . . . . .	12
<b>3</b>	<b>Case set-up</b>	<b>13</b>
<b>4</b>	<b>Design of inductive charging system</b>	<b>15</b>
4.1	Overview of system . . . . .	15
4.2	Design of power pads . . . . .	15
4.2.1	Calculations of inductance . . . . .	16
4.3	Circuit parameters . . . . .	17
4.3.1	Self and mutual inductance . . . . .	17
4.3.2	Coil resistance . . . . .	18
4.3.3	Capacitor banks . . . . .	19
4.3.4	DC-link capacitor . . . . .	19
4.4	Circuit simulations . . . . .	19
4.5	Construction of system and components . . . . .	21
4.5.1	Power pads . . . . .	21
4.5.2	Capacitors and diodes . . . . .	21
<b>5</b>	<b>Measurement set-up</b>	<b>25</b>
5.1	Lab set-up . . . . .	25
5.2	Experimental determination of parameters . . . . .	25

5.2.1	Self inductance . . . . .	25
5.2.2	Mutual inductance . . . . .	26
5.2.3	Capacitance of capacitors . . . . .	26
5.3	Voltage, current and magnetic field measurements . . . . .	26
<b>6</b>	<b>Results and analysis</b>	<b>27</b>
6.1	Comparison between measured and simulated inductance . . . . .	27
6.2	Wave shapes . . . . .	28
6.2.1	Switching waveforms of MOSFET . . . . .	29
6.3	Comparison between simulations and measurement . . . . .	30
6.3.1	Frequency behaviour . . . . .	31
6.3.2	Power transfer and efficiency . . . . .	32
6.3.3	Losses in system . . . . .	32
6.4	Misalignment and change in air gap . . . . .	34
6.4.1	Misalignment between power pads . . . . .	34
6.4.2	Change in air gap . . . . .	34
6.5	Heat dissipation . . . . .	35
6.6	Magnetic field . . . . .	36
<b>7</b>	<b>Conclusions</b>	<b>39</b>
7.1	Future work . . . . .	39
	<b>Bibliography</b>	<b>41</b>

# 1

## Introduction

In this chapter a background to the project is presented as well as previous work in the area. The aim and purpose of the project is also presented.

### 1.1 Background

Today inductive charging is used in a wide variety of applications. One example is charging of smart-phones. An increasing number of phone-manufacturers offers power-pads for their smart-phones making it easy and convenient for customers to charge their cellphones.

Inductive charging also have advantages in industrial applications, for example when the condition is either wet, dirty or objects are moving. Without cables one can charge moving objects easy, charge sealed products and charge products in wet environments without having to deal with the problem cables possess [1].

Furthermore, inductive charging has the ability to become a feasible option in charging of electric vehicles. The industry of electric vehicles is growing and the electric car is starting to become a feasible option to the standard combustion driven vehicle. It is therefore relevant to continue with the development of inductive charging to improve the user experience.

With inductive charging of electric vehicles, the driver does not have to exit their vehicle to plug in a cable when charging. The driver could park the car over an inductive charging pad or charge the car while driving on an inductive charging lane.

Inductive power transfer (IPT) systems uses a high frequency power supply. This is needed because in IPT systems the coupling between the coils are relatively low compared to transformers, which often has small air gaps or magnetic core leading the magnetic fields.

To make wireless charging a feasible solution for electric vehicles, interoperability is needed. For example, regarding the coils, it is important that electric vehicles from two different manufactures can be charged on the same charging pad. Furthermore, a standardisation of operating frequency, power levels and misalignment tolerance is needed between the different industries. In 2014 the SAE International decided that the power supply frequency should be between 81.38 - 90  $kHz$  [2].

### 1.2 Previous work

The Oak Ridge National Laboratory (ORNL) which is the largest department of science and energy laboratory in US has developed a wireless charging system for electric vehicles. The inductive charging system transfers 20 *kW* with an efficiency of 90 %. The project has been ongoing for approximately three years and was presented at March 31, 2016. ORNL's electrical power department are now aiming for a 50 *kW* wireless charging system [3].

Dr. P Bauer and S Chopra from Delft University of Technology, the largest University of Technology in The Netherlands, developed an inductive charging system in 2011. It was a 100 *W* system with an efficiency of 83 % for a 5 *cm* air gap [4].

In 2015 an inductive charging system for small electric vehicles was developed as a master's thesis work at Chalmers University of Technology. The charging system transfers 1100 - 1200 *W* at 5 *cm* air gap with the efficiency of 84 % [5].

### 1.3 Purpose

In this master thesis work an IPT system will be designed for Aros Electronics self-balancing robot. The principle of designing an IPT system for this robot is the same as for example, IPT systems for electric vehicles. Therefore this project is relevant as the Aros robot is in need of wireless charging and also since the IPT system could be rescaled and applied in other areas and projects.

Furthermore, this master thesis work is of importance because a complete IPT system should in the future be developed and implemented in Aros Electronics self-balancing robot, requiring specific requirements. Size is of importance as the power pad on the secondary side should be able to fit inside of the robot. The system should also be designed to be tolerant for misalignment between the power pads, since the robot in the future should be able to find the charging pad itself and the precision of the parking for the robot is unknown.

The aim of this project is to develop an IPT system that can transmit 150 *W* over a 3 *cm* air gap. The efficiency of the IPT system should exceed 80 %.

# 2

## Theory

In this chapter the theory that this project is founded on is presented.

### 2.1 Inductive power transfer

In this section the theory of the IPT is presented. The concept of mutual inductance and coupling factor is presented as well as the need for high frequency and capacitive compensation in an IPT system.

#### 2.1.1 Mutual inductance and coupling factor

In 2.1 two closed loops are presented,  $C_1$  and  $C_2$ , each enclosing a surface,  $S_1$  and  $S_2$ . If the first loop is excited with a time-varying current,  $I_1$ , a magnetic flux density,  $B_1$ , will be produced. The part of the magnetic flux density that passes through the surface enclosed by the second loop,  $S_2$ , is called the mutual flux,  $\Phi_{12}$ . The mutual flux can be calculated as

$$\Phi_{12} = \int_{s_2} B_1 dS_2 \quad [Wb] \quad (2.1)$$

Furthermore, if instead only the second loop is excited with a time-varying current,  $I_2$ , the resulting mutual flux can be calculated as

$$\Phi_{21} = \int_{s_1} B_2 dS_1 \quad [Wb] \quad (2.2)$$

where  $\Phi_{21}$  is the mutual flux and  $B_2$  the magnetic flux density produced by  $I_2$ .

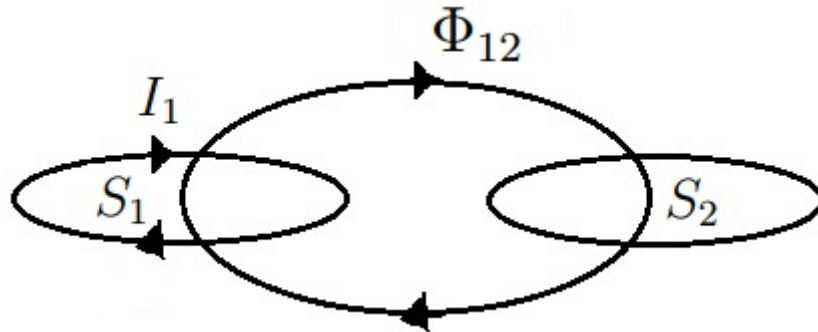


**Figure 2.1:** Two closed loops  $C_1$  and  $C_2$

The magnetic flux density is proportional to the current accordingly to Biot-Savarts law and thus the current is proportional to the mutual flux as well. The proportional constant is called mutual inductance,  $L_{12}$ , and the relation is thus as follows

$$\Phi_{12} = L_{12}I_1 \quad [Wb] \quad (2.3)$$

If the second coil has more than one turn, the flux linkage,  $\Psi_{12}$ , is defined as

$$\Psi_{12} = N_2\Phi_{12} \quad [Wb] \quad (2.4)$$

where  $N_2$  is the number of turns of the second coil.

The flux linking with  $C_2$  when  $C_1$  is excited and vice versa are the same and thus

$$M = L_{12} = L_{21} \quad [H] \quad (2.5)$$

where  $M$  is denoted as the mutual flux.

The total flux that is produced when the first loop is excited is called the self-inductance,  $L_1$ . The part that will not link with the second coil is called leakage inductance,  $L_{1\sigma}$  [6]. Therefore the self-inductance can be presented as

$$L_1 = L_{1\sigma} + M \quad [H] \quad (2.6)$$

If instead the second loop is excited the self-inductance of second loop can be described by

$$L_2 = L_{2\sigma} + M \quad [H] \quad (2.7)$$

The coupling factor,  $K$ , is a measure of how good the magnetic coupling is between the two coils and can be calculated as

$$K = \frac{M}{\sqrt{L_1 L_2}} \quad (2.8)$$

where  $L_1$  primary inductance and  $L_2$  is the secondary inductance [7].

With the second loop arranged as an open circuit and the first loop excited with the time-varying current  $I_1$ , the induced voltage in the secondary loop can be expressed as

$$V_{ind} = j\omega M I_1 \quad [V] \quad (2.9)$$

where  $V_{ind}$  is the induced voltage in the secondary loop and  $\omega$  the angular frequency of the current  $I_1$ .

In IPT systems, the air gap between the coils are relative large compared to that in a transformer. Furthermore, there is no transformer core leading the magnetic fields between the coils. This result in lower mutual inductance for IPT systems compared to transformers. In order to maintain the same induced voltage on the secondary side with an decreasing mutual inductance the frequency or the current has to be

increased according to (2.9). A higher current will lead to more resistive losses as well as more stress on the inverter. This clearly demonstrate the importance of high frequency in IPT systems [8].

### 2.1.2 Inductive power transfer model

In an ideal transformer the coupling coefficient is 1 and there is no leakage flux. Transformers have a relative high coupling between the coils as the air gaps are often small and the transformer core leads the magnetic fields.

However, an IPT system can be represented as a transformer with a low coupling factor. In 2.2 a basic model of the transformer is presented, where  $K$  is the coupling factor,  $R_1$  the winding resistance of the primary coil and  $R_2$  the winding resistance of the secondary coil,  $R_L$  the resistive load and  $V_1$  the sinusoidal input voltage [9].

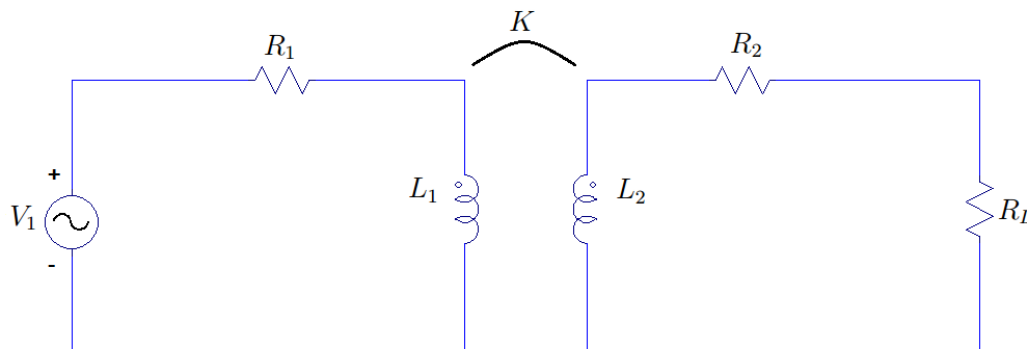


**Figure 2.2:** Basic model of transformer

### 2.1.3 Misalignment between coils and change in air gap

The mutual inductance is inversely proportional to the length between the coils as well as the shared area of the two coils. In 2.3 and 2.4 four different relations regarding air gap, misalignment and diameter of the coils are presented. In an IPT system the distance between the transmitting coil and the receiving coil is often large and this is represented in 2.3b. This will result in less magnetic flux linking with the receiving coil compared to the two coils in 2.3a. This results in lower mutual inductance for the coils in 2.3b and thus lower coupling factor.

If there is a misalignment between the receiving and transmitting coil as presented in 2.4a the coupling will also be lower compared to 2.3a. There will also be lower coupling between the two coils if the receiving coil would have a smaller diameter as in 2.4b. Less flux from the transmitting coil will link with the receiving coil and

result in less mutual flux. However, 2.4b compared to 2.3a allows for more misalignment before the coupling is lowered substantially or lost.

Loosely coupled systems will result in lower efficiency in the power transferred between the two coils, resulting in more heat and electromagnetic emissions as the leakage flux increases. When designing an IPT system there is a conflict between high efficiency and large air gaps for the energy transfer [10].

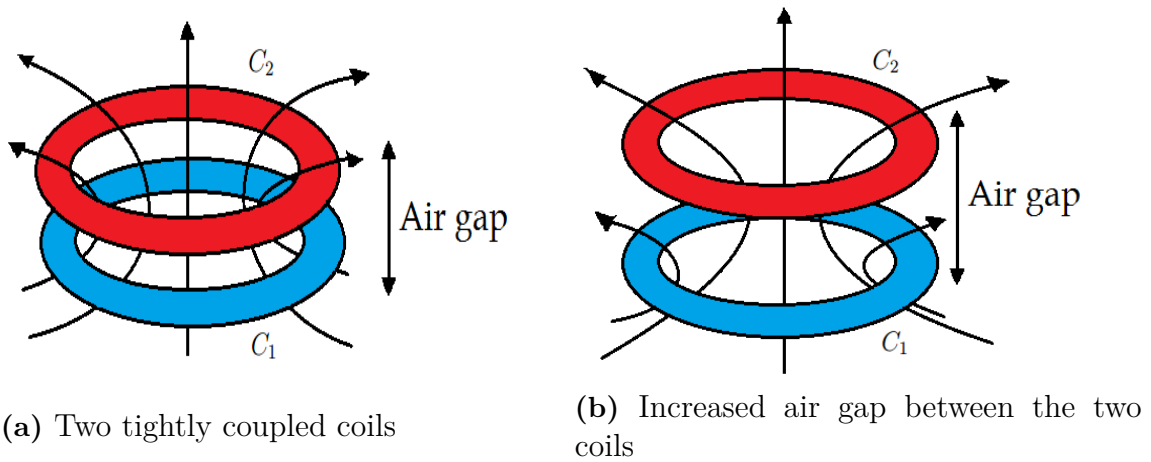


**Figure 2.3:** Flux lines between two coils. The blue coil is the transmitting coil and the red coil is the receiving coil.

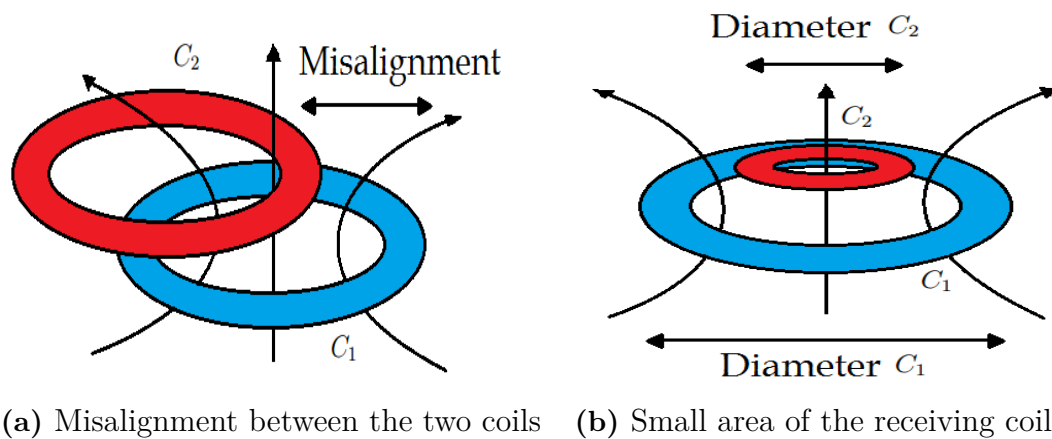


**Figure 2.4:** Flux lines between two coils. The blue coil is the transmitting coil and the red coil is the receiving coil.

### 2.1.4 Resonant circuits

Capacitive compensation in IPT systems is used to increase power transfer and efficiency. There exists four different compensation topologies; series-series compensation, series-parallel compensation, parallel-series compensation and parallel-parallel

compensation. The secondary winding is compensated with the capacitance;  $C_2$ , independent of its placement in series or parallel as the relation

$$C_2 = \frac{1}{w_0^2 L_2} \quad [F] \quad (2.10)$$

describes. Where  $w_0$  is the secondary side resonance frequency and  $L_2$  the secondary coil inductance.

Depending on the compensation topology there are four different ways to calculate the primary capacitance  $C_1$ . However, series-series compensation as seen in 2.6 is the most efficient and reliable compensation topology because the secondary resonance winding transformed to the primary winding only has a real part, resulting in a higher power factor. Series-series compensation is also independent of the mutual inductance and the load. With these advantages that series-series compensation has it is mostly used in battery charging systems. Therefore series-series compensation is used in this project, as it is independent of the load and the orientation of coils.

The transfer function,  $H$ , when the primary resonance frequency equals the secondary resonance frequency for the series-series compensated system recalculated to the primary side is

$$H = \frac{nV_2}{V_1} = \frac{R_L s^3 C_1 \frac{C_2}{n^2} M}{R_L \frac{s C_2}{n^2} (1 + s^2 C_1 (M + L_{1\sigma})) + (1 + s^2 C_1 L_{1\sigma})(1 + s^2 C_1 (L_{1\sigma} + 2M))} \quad (2.11)$$

where  $s$  is the Laplace-domain variable,  $R_L$  is the load,  $C_1$  is the primary side capacitance,  $M$  the mutual inductance,  $L_{1\sigma}$  the primary leakage inductance,  $n$  the winding turn ratio,  $V_2$  the output voltage and  $V_1$  the input voltage.

Here  $L_{1\sigma}$  is calculated as

$$L_{1\sigma} = (1 - K)L_1 \quad [H] \quad (2.12)$$

where  $K$  is the coupling factor and  $L_1$  the primary inductance.

From this transfer function there are three resonance frequencies;  $w_1$ ,  $w_2$  and  $w_3$  as the three equations

$$w_1 = \frac{1}{\sqrt{C_1(2M + L_{1\sigma})}} \quad [rad/s] \quad (2.13)$$

$$w_2 = \frac{1}{\sqrt{C_1 L_{1\sigma}}} \quad [rad/s] \quad (2.14)$$

$$w_3 = \frac{1}{\sqrt{C_1(M + L_{1\sigma})}} \quad [rad/s] \quad (2.15)$$

describes. In 2.5 the frequency response for the transfer function for different loads can be seen. When the load becomes low enough the phenomenon of bi-furcation

appears. Here there are three resonance frequencies instead of one where  $w_1 < w_3 < w_2$ . At  $w_1$  the input voltage becomes equal to the reflected output voltage  $nV_1$  since the transfer function is in unity. At the second resonance frequency the transfer function is also in unity. At the third frequency the function behaves like a voltage divider. The voltage gain depends on the load,  $R_L$ . At this frequency the full bridge inverter usually operates at because of the high efficiency and power output capability [11], [12].

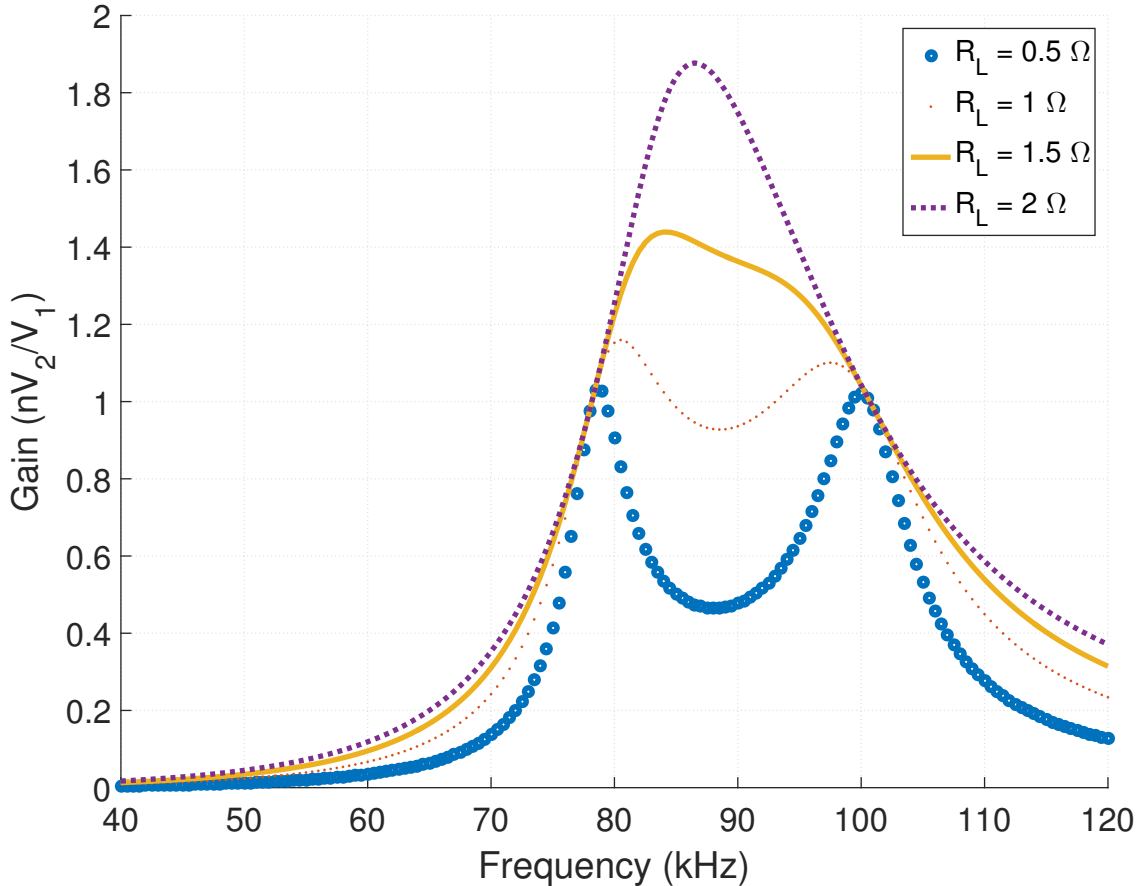


**Figure 2.5:** The frequency response for the transfer function  $H$  for different loads. Here  $C_1 = 282$  nF,  $C_2 = 422$  nF,  $L_1 = 12.43$   $\mu$ H,  $L_2 = 8.31$   $\mu$ H,  $M = 2.92$   $\mu$ H and  $n = 1$ .

By rewriting (2.15), where the system is supposed to operate, with (2.10) the primary capacitance is then calculated with the resulting equation

$$C_1 = \frac{L_2 C_2}{L_1} \quad [F]. \quad (2.16)$$

## 2.2 DC to AC inverter

In this section the structure of the inverter and its switching mode is presented which is used in this project to produce a high frequency square-wave voltage.

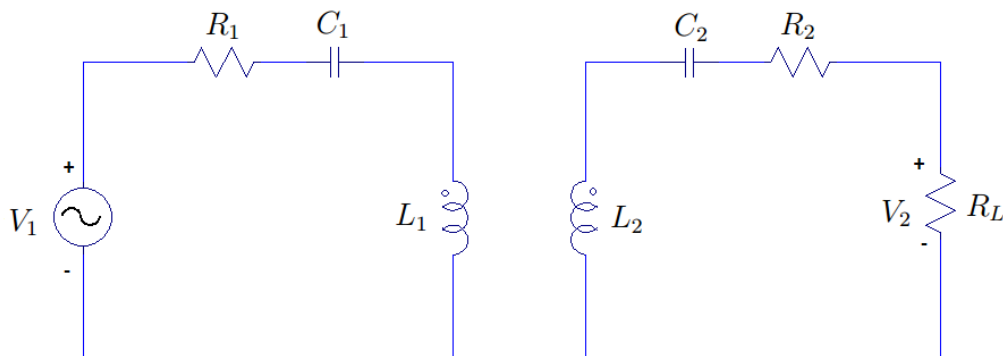


**Figure 2.6:** Series-series capacitive compensation

To be able to control the rms voltage with voltage cancellation in a full bridge inverter unipolar switching scheme is the only mode possible [13].

### 2.2.1 Single phase full bridge inverter

The structure of a full bridge inverter can be seen in figure 2.7a. Unipolar switching-mode is used and is generated by controlling each leg separately on the full bridge inverter. The control is done by comparing a carrier wave against two triangular waves which can be seen in 2.7b. The triangular waves are 180 degrees out of phase to each other. When  $V_{control}$  in 2.7b is greater or less than the triangular wave,  $V_{tri1}$ , switch  $T_{A-}$  or  $T_{A+}$  is triggered. The same applies for  $V_{control}$  compared to  $V_{tri2}$  but it controls switch on the other leg,  $T_{B-}$  and  $T_{B+}$ . This switching scheme creates four different states in which the switches operate;  $(T_{A+}, T_{B-})$ ,  $(T_{A-}, T_{B-})$ ,  $(T_{A+}, T_{B+})$ ,  $(T_{A-}, T_{B+})$ .

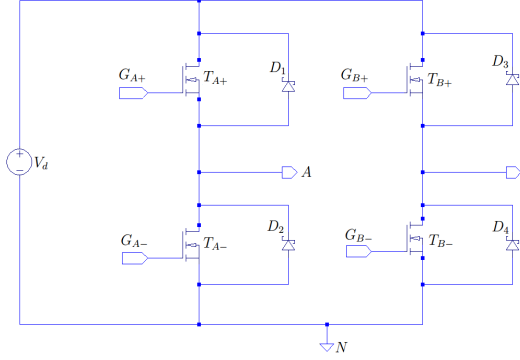
Between two switching states there is a moment called blanking time. During this time none of the two switches on one leg are opened. This is to ensure that there is no short circuit on a leg. With a current stiff load the current will continue its direction and go through the diode on the MOSFET to be triggered each time a state changes.

The switching scheme results in the phase voltage seen in 2.8a, where the width of the pulses is controlled by changing the magnitude of the carrier wave. The applied voltage over the load (voltage over phase A and B in 2.7a) can then be seen in 2.8b. The angle which the voltages  $V_{BN}$  and  $V_{AN}$  overlaps is called over lap angle,  $\alpha$ , and can be seen in 2.8b. The over lap angle controls the rms voltage,  $V_{RMS}$ , applied to the load as

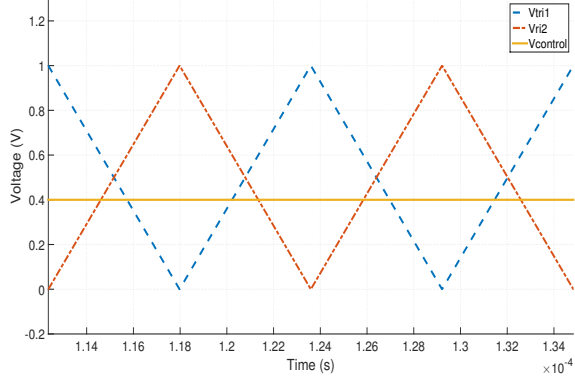
$$V_{RMS} = V_{DC} \left(1 - \frac{\alpha}{\pi}\right) \quad [V] \quad (2.17)$$

where  $V_{DC}$  is the DC voltage ( $V_d$  in 2.7a) converted to AC [14]. Alpha can be re-expressed as *Duty cycle* with

$$Duty\ cycle = \frac{\pi - 2\alpha}{2\pi} \quad (2.18)$$

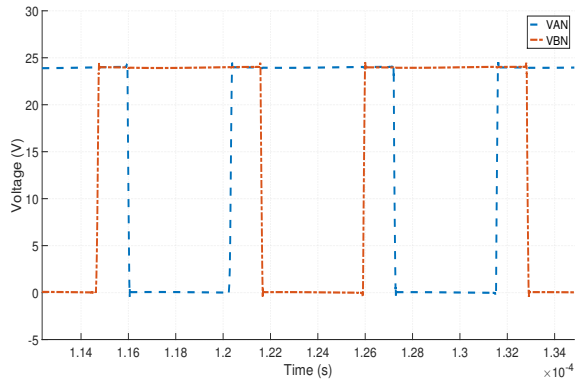


(a) Single phase full bridge inverter.

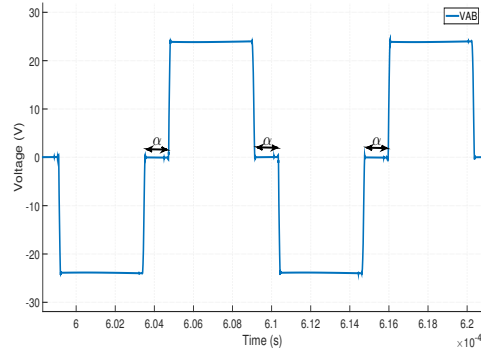


(b) The triangular waves and the carrier wave.

**Figure 2.7:** The inverter and its control waves.



(a) Voltage  $V_{AN}$  and  $V_{BN}$ . The nodes A, B and N can be seen in 2.7a



(b) Voltage  $V_{AB}$  between leg A and B of the inverter. The nodes A, B can be seen in 2.7a

**Figure 2.8:** The resulting output voltages between the nodes seen in 2.7a.

### 2.2.1.1 Conduction and switching losses

The losses occurring for the full bridge inverter are switching losses and conduction losses for the MOSFETs. The conduction losses,  $P_{conduction}$ , are equal to

$$P_{conduction} = I_D^2 R_{DS,on} \quad [W] \quad (2.19)$$

where  $I_D$  is the current passing from source to drain and  $R_{DS,on}$  is the drain to source resistance. For high switching frequencies the conduction losses becomes small compared to the switching losses. The turn on and off characteristics depends on the gate resistance and the parasitic capacitance between gate to source and gate

to drain;  $C_{GS}$  and  $C_{GD}$ .

The switching characteristics for a typical power MOSFET can be seen in 2.9. During turn on and turn off the gate current and gate-source voltage reaches close to its final value during the time period  $t_{c,on}$  and  $t_{c,off}$ , where the index c stands for crossover. The majority of the instantaneous switching loss,  $P_{Switch}(t)$ , occurs during these time periods as

$$P_{Switch}(t) = I_D(t)V_{DS}(t) \quad [W] \quad (2.20)$$

where  $I_D(t)$  and  $V_{DS}(t)$  are the drain to source current and voltage [15], [16].

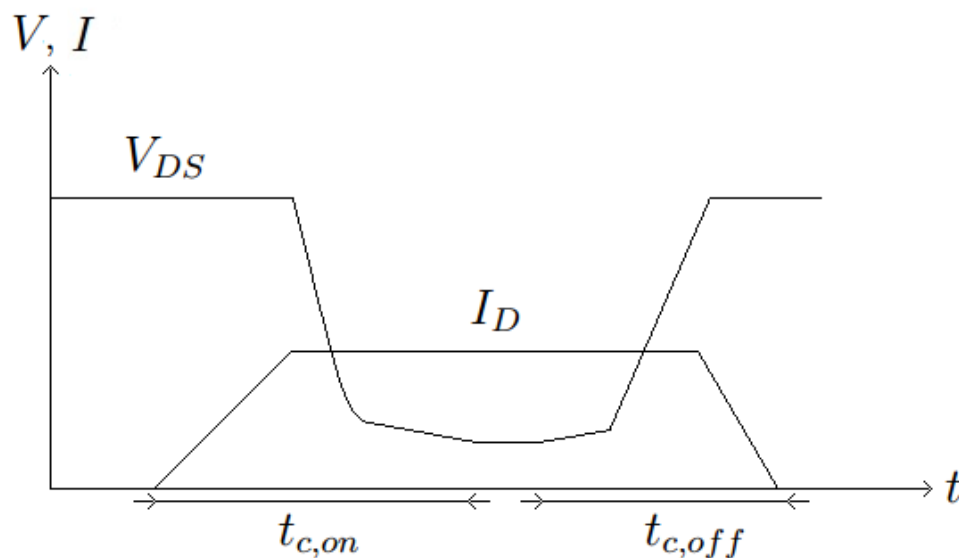


**Figure 2.9:** The turn on and turn off state of a typical MOSFET were voltage and current are presented.

## 2.3 AC to DC rectifier

In this section the rectifying bridge used in this project is presented. The rectifying bridge is placed on the secondary side of the IPT system and is used to deliver a DC-voltage to the battery charging side.

### 2.3.1 Single phase diode bridge rectifier

The full bridge diode rectifier in 2.10 converts alternating current to positive current. The diodes, D1, D2, D3 and D4 can only conduct positive currents which forces the DC-sided current to ripple between its magnitude and zero with the double

frequency. The rectified DC-voltage,  $V_d$ , equals, for a sinusoidal incoming voltage and continuous current,

$$V_d = 0.9V_{source} \quad [v] \quad (2.21)$$

where  $V_{source}$  is the rms input voltage. With a DC-link capacitor,  $C_d$ , the positively rippling voltage rectifies. The capacitance can be chosen with the empirically derived formula

$$C_d = \left( \frac{8.6}{f \cdot R \cdot \%ripple} \right) \quad [F] \quad (2.22)$$

where  $f$  is the frequency,  $R$  is the load resistance and  $\%ripple$  is the maximum allowable ripple in percent [17], [18].

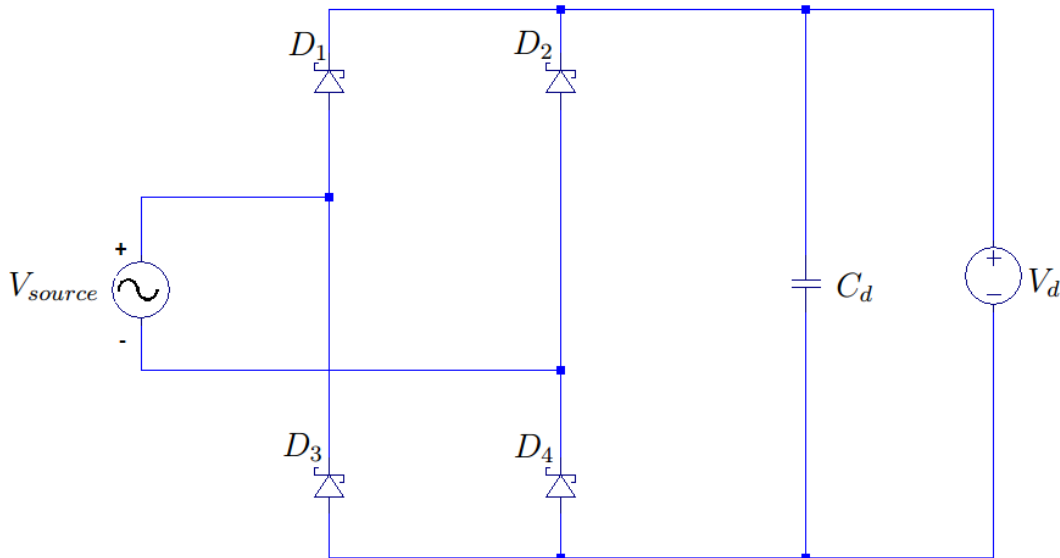


**Figure 2.10:** Single phase diode bridge rectifier

### 2.3.1.1 Conduction losses

The conduction losses for a diode during forward conduction in the bridge rectifier can be expressed as

$$P_{conduction} = V_{th}I_{av} + R_d I_{rms}^2 \quad [W] \quad (2.23)$$

where  $V_{th}$  is the threshold voltage for the diode to start conducting,  $I_{av}$  is the average forward current,  $I_{rms}$  the rms current and  $R_d$  the forward slope resistance. Both  $R_d$  and  $V_{th}$  is temperature dependant which causes the losses to increase with increasing temperature for high currents. If the reverse recovery time for the diodes is small, the forward conduction region can be regarded as the majority cause for conduction loss [19].

# 3

## Case set-up

The distance between the self-balancing robot's bottom and ground decreases when moving, compared to standstill. This is because of the angle shift between the bottom and the ground. Therefore the air-gap was chosen to be 3 *cm* so that the robot can enter the charging pad without hitting it.

The batteries of the robot is placed inside an opening of the robot's bottom of 15x15 *cm*<sup>2</sup>. Therefore the receiving charging pad should be able to fit inside this opening and thus the receiving charging pad cannot exceed 15x15 *cm*<sup>2</sup>. The distance between the ground and the robot is 15 *cm*. Therefore a stand for the transmitting charging pad will have to be built in the future in order to achieve the desired air-gap between the power pads.

In the future the self-balancing robot should be able to find the transmitting charging pad by it self. Without knowing the precision of the parking of the robot there may be some misalignment between the coils. Therefore a test-stand for the two power pads have been designed in order to be able to make measurements with different misalignment's as well as changes in the air gap.

The batteries to be charged are lithium-ion batteries. Therefore the cells needs to be monitored and balanced. There are two packages of lithium-ion batteries used in the robot and therefore two chargers with battery management systems (BMS) will be used. The chargers maximum input power is 50 *W* each resulting in 100 *W*. Therefor the aim is to transfer 150 *W* with a perfect square wave with a duty-cycle of 50 %. This to have a safety margin and also since the charger may be replaced in the future making it possible to charge with more power. The DC input voltage to the chargers are 11 - 18 *V*.

For this task a full bridge inverter with a DC-voltage input of 24 *V* is used. This inverter is provided by Aros Electronics. The controlling of the switches by the gate drivers should be designed and implemented in the processor.



# 4

## Design of inductive charging system

In this chapter the design of the inductive charging system is presented. The simulations and components used are presented and justified.

### 4.1 Overview of system

The complete inductive charging system to eventually be implemented in Glenn can be seen in 4.1.

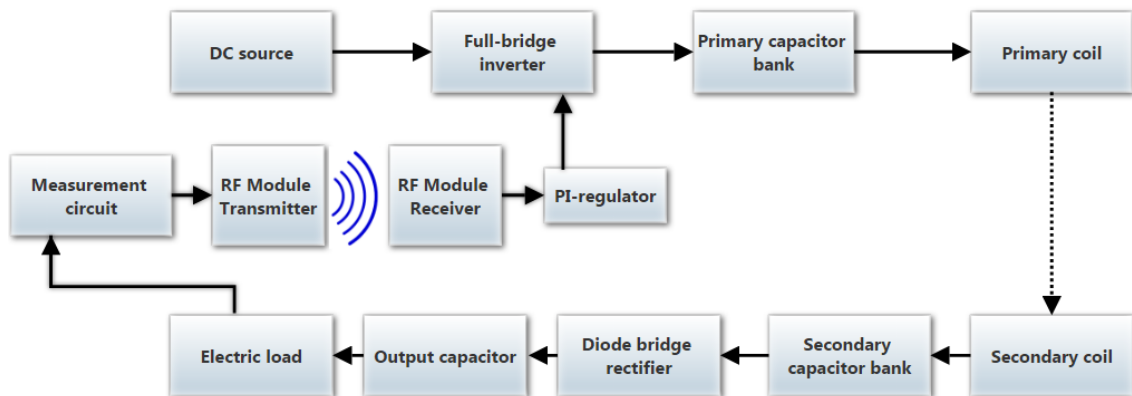


**Figure 4.1:** Overview of the inductive charging system

The focus in this project is on the whole system except the wireless feedback implementation containing measurement circuit, radio frequency (RF) modules and PI-regulator seen in 4.1.

### 4.2 Design of power pads

To design the two coils different parameters were taken into consideration. The minimum air gap specified in the case set up is 3 cm. With an increasing air gap the cross-sectional area of the two coils has to increase in order to not decrease the coupling factor. With a maximum limit on the area of the receiving power pad the

air gap was chosen to be 3 *cm* to not result in a too low coupling factor.

The coils were chosen to be radially wound rather than vertically (on top of each other). The reason for is because when radially wound all the turns will come close to the surface of the ferrite. This results in more magnetic field enclosed by the ferrite and thus less leakage flux. Furthermore, the cross-sectional area between the two coils increases which increases the tolerance for misalignment.

A layer of ferrite plates underneath the transmitting coil and above the receiving coil was implemented. Simulations were conducted with and without ferrite to verify the effect of ferrite plates on the self-inductance and mutual inductance. The ferrite plates leads the magnetic field resulting in lower leakage flux and thus higher mutual inductance. To make sure that the ferrite engulfs the magnetic field properly the radius of the ferrite plates is chosen to be larger than the coils radius. The difference in coupling factor between coils with ferrite and without is presented in Table 4.2.

To minimise the effect of misalignment between the coils, the transmitting coil is chosen to be larger than the receiving coil. With a larger transmitting coil the effective cross-sectional area between the two coils will not change as much when misaligned.

The frequency for the supply voltage from the inverter is chosen to be 85 *kHz*. This frequency was chosen as a high frequency is needed and since this frequency is within the SAE International restrictions as well as the inverter specifications provided by Aros Electronics.

### 4.2.1 Calculations of inductance

To calculate the self-inductance of the coils in COMSOL the stationary domain is used in magnetic field mode. The solver used is the 2D axisymmetric solver, which creates a 3D model by rotating the 2D model 360 degrees. This solver uses less data storage and computational time over the 3D solver. COMSOL solves the problem numerically by calculating the total energy induced in the system within the designed boundaries. The total energy,  $W_m$ , is calculated as

$$W_m = \iiint_V \frac{1}{2} H \cdot B \, dv = \iiint_V \frac{B^2}{\mu} \, dv \quad [J] \quad (4.1)$$

where  $H$  is the magnetic field strength and  $B$  is the magnetic flux density enclosed by the volume  $V$  and  $\mu$  the permeability. Then the relation between magnetic energy stored in an inductor and the inductance,  $L$ , can be used by rewriting

$$W_m = \frac{1}{2} LI^2 \quad [J] \quad (4.2)$$

to

$$L = \frac{2W_m}{I^2} \quad [H] \quad (4.3)$$

which completes the calculation COMSOL executes in order to find the inductance for the coil that is excited with the current  $I$ .

To calculate the mutual inductance,  $M$ , for the two coils the receiving coil is open circuited while the transmitting coil is excited with a  $85\text{ kHz}$  current. The only physical quantity linking the two coils together is accordingly the flux through the open circuited coil from the excited coil. This relation is described with

$$\Psi = MI \quad [Wb] \quad (4.4)$$

and by using the definition of Faraday's law of induction and by solving if for induced voltage,  $V_{oc}$ , the equation can be rewritten as

$$M = \frac{jV_{oc}}{wI} \quad [H] \quad (4.5)$$

where  $w$  is the angular velocity which COMSOL uses to calculate the mutual inductance for the system [20].

### 4.3 Circuit parameters

The final design used for the coil configuration can be seen in 4.2. The air gap is  $3\text{ cm}$ , the transmitting coil has a diameter of  $11.8\text{ cm}$  and the receiving coil a diameter of  $8\text{ cm}$ . Before reaching this design a multiple of coil designs were tested with their corresponding resonance capacitance calculated from (2.10) and (2.15). The test conducted compared the power transfer and efficiency using the circuits seen in 4.3 and 4.4 from LTspice. This design were chosen because it could transmit  $160\text{ W}$  at  $85\text{ kHz}$  with  $50\%$  duty-cycle to the load, with  $87\%$  efficiency.

#### 4.3.1 Self and mutual inductance

The simulated inductance without the linking power pad is presented in Table 4.1, these are the coils separate-self inductance. When the receiving power pad is placed  $3\text{ cm}$  above the transmitting power pad the inductance of the transmitting power pad is affected by the ferrite from the receiving power pad and vice verse. These inductance's simulate the systems inductance's with a perfect alignment and is presented in Table 4.2.

With ferrite the inductance increases and also the coupling factor. This can be seen in Table 4.2 where the coupling factor,  $K$ , is calculated for both with and without ferrite attached to the coils.

Furthermore, to note is that the ferrite from the transmitting pad affects the receiving pads self-inductance and vice verse. This can be seen by comparing Table 4.1 and 4.2.

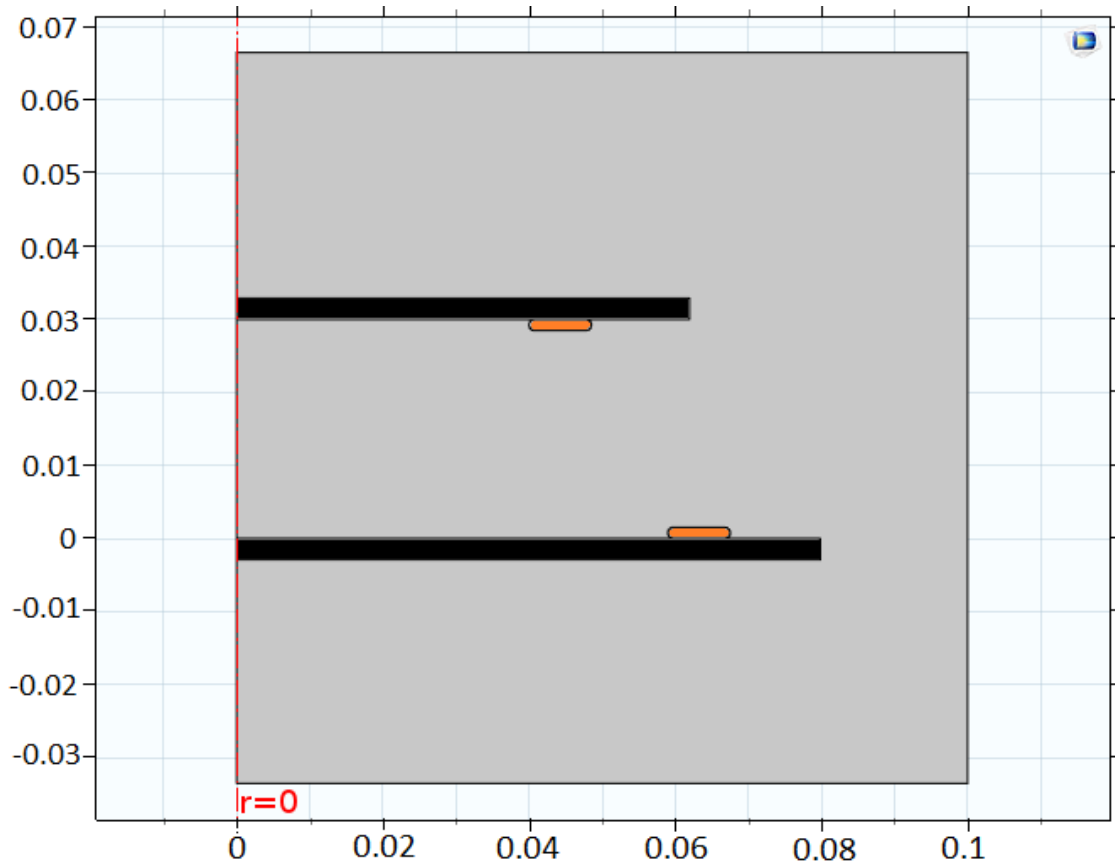


**Figure 4.2:** 2D axisymmetric geometry design in COMSOL used to calculate mutual and self inductances. Where the grey area is air, the orange areas represents the cross-sectional area of the wires and the black areas represents the ferrite plates.

The litz wire dimensions was chosen with respect to the previous work done at Chalmers where they recommended the use of a litz wire with a smaller strand diameter than  $0.2 \text{ mm}$  and more than 180 strands to reduce the skin effect and proximity effect. Therefore a litz wire with 240 strands with  $0.1 \text{ mm}$  diameter for each strand were chosen.

**Table 4.1:** Self-inductances of the transmitting and receiving coils without influence of the ferrite in the opposite coil.

	Measurement	COMSOL
Parameter	With ferrite	With ferrite
L1 [ $\mu H$ ]	11.45	11.97
L2 [ $\mu H$ ]	8.08	7.67

### 4.3.2 Coil resistance

The litz wire was chosen so that the frequency would have small to no effect of the skin effect and proximity effect therefore the resistance for the wire was approxi-

**Table 4.2:** Inductances obtained from COMSOL simulations. Self inductances calculated with influence of ferrite from opposite power pad.

Parameter	With ferrite	Without ferrite
L1 [ $\mu$ ]	12.43	6.85
L2 [ $\mu$ ]	8.31	4.30
M [ $\mu$ ]	3.78	1.13
K	0.37	0.21

mated to its DC-resistance. The resistance of the wire was estimated by regarding the litz wire as a solid circular conductor with the diameter of the total 240 strands as,  $D_{Litz-wire}$ ,

$$D_{Litz-wire} = \sqrt{D_{strand}^2 N_{strands}} \quad [m] \quad (4.6)$$

where  $D_{strand}$  is the diameter of a single strand and  $N_{strands}$  are the total number of strands. The total length of the litz wire,  $l_{Litz-wire}$ , is then estimated by adding the length for each lap as

$$l_{Litz-wire} = \sum_{n=1}^{n_{turns}} D_{inner} + \frac{D_{Litz-wire}}{2} n_{turns} + D_{Litz-wire} (n_{turns} - 1) \quad [m] \quad (4.7)$$

describes, where  $D_{inner}$  is the inner diameter for the coil and  $n_{turns}$  is the number of turns for the wire. The coil length for the transmitting coil is then calculated to 190 *cm* and for the receiving coil to 130 *cm*. The DC resistance for the transmitting and receiving coil is then calculated to 0.017  $\Omega$  and 0.0119  $\Omega$  respectively.

### 4.3.3 Capacitor banks

The resonance circuits capacitance's for the transmitting side and receiving side were calculated with (2.15) and (2.10). The capacitance's was calculated with the simulated values with ferrite seen in Table 4.2 and for 85 *kHz* to 422 *nF* and 282 *nF* for the transmitting and receiving side.

### 4.3.4 DC-link capacitor

The DC-link capacitance was calculated from (2.22) to 33  $\mu F$ . The accepted voltage output ripple was chosen to 3% of the load voltage at a load of 1  $\Omega$  at 85 *kHz*.

## 4.4 Circuit simulations

All the circuit simulations were made in the simulation program LTspice. The full bridge inverter in 4.3 simulates the inverter Aros Electronics provided the project with. The circuit in 4.4 represents the IPT with series-series compensation, diode bridge rectifier and a battery load. All the parameters in the circuit are obtained from simulations and calculations. The diodes in the simulation were chosen to be

Schottky diodes with an average forward current of 10 A.

The MOSFETs has built in diodes which removes the need for extra diodes in the inverter design. The capacitor  $C_{DC}$  is the DC-DC capacitor that is included in the Aros inverter card.

The inverter produces a square wave voltage over the resonance circuit. The reason for not using a sinusoidal PWM voltage is the switching frequency. For a sinusoidal waveform PWM switching is needed, which requires much higher switching frequency which is not possible for the MOSFETs provided by Aros.

In 4.4 a 12 V battery on the receiving side is represented with a 12 V voltage source and a series resistance,  $R_{battery}$ . However, for all the simulations in chapter 6 a load having 1.15  $\Omega$  and 56  $\mu H$  was used.

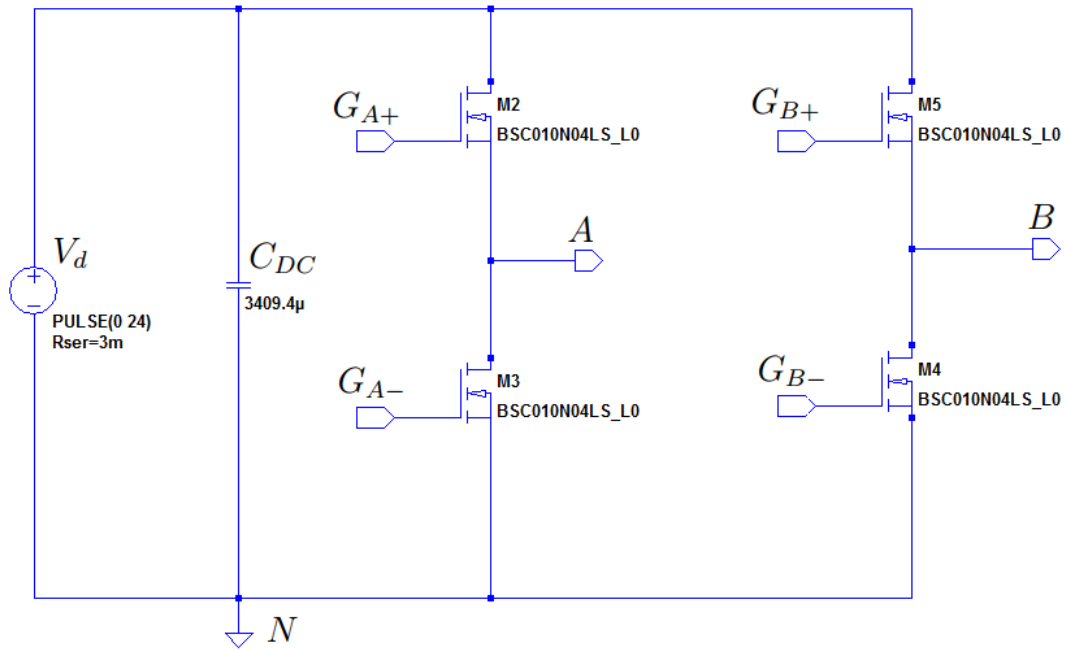


**Figure 4.3:** Single phase full bridge inverter used in LTspice.

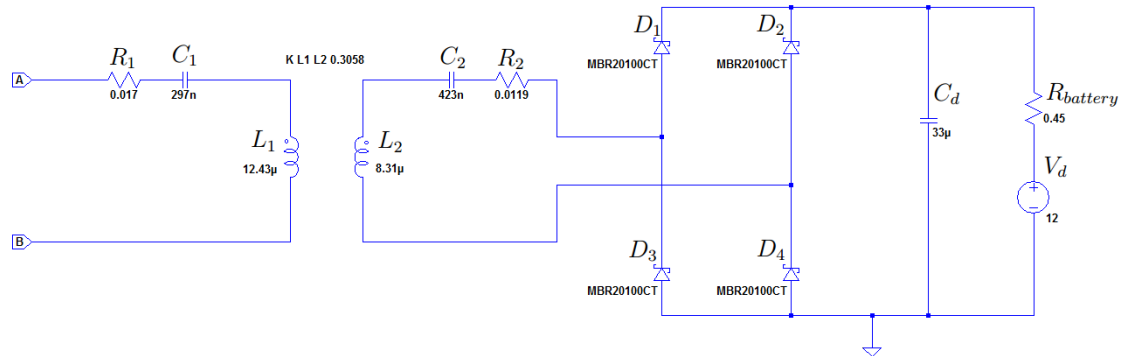


**Figure 4.4:** Circuit in LTspice representing the IPT with series-series compensation, diode bridge rectifier and battery load.

## 4.5 Construction of system and components

From the chosen design and simulated parameters in the previous section the system is then constructed which is described in the following section.

### 4.5.1 Power pads

The litz wire on the transmitting and receiving side were wound on a piece of 3D-printed plastic with an height equal to the litz wires diameter. Each coil were wounded and glued 5 laps around its axis as seen in 4.5. The coils were then mounted upside down on the ferrite layouts seen in 4.6 to create the final power pads used in system. The litz wires was twisted around its axis to minimize the proximity and skin effect.

The volume of the ferrite plates on the transmitting and receiving side matches the volume used in the simulations. However, in the simulations two perfect cylinder-shaped ferrite layouts are used. The same geometry was not possible to build with the ferrite blocks used. Therefore two layouts were constructed with the same volume, that covers the coils with an extra marginal, to ensure that the magnetic field is enclosed properly.

### 4.5.2 Capacitors and diodes

When creating the capacitor bank for the transmitting and receiving side nine smaller capacitors was put in parallel on each side. The capacitors on the transmitting side was  $47\text{ nF}$ ,  $630\text{ V}_{DC}/400\text{ V}_{AC}$  and on the receiving side  $33\text{ nF}$ ,  $630\text{ V}_{DC}/400\text{ V}_{AC}$ , both with polypropylene di-electric. This resulted in  $423\text{ nF}$  on the transmitting side and  $297\text{ nF}$  on the receiving side. The total capacitance would be as close to the simulated value as possible and to be able to handle the rms voltage

#### 4. Design of inductive charging system

---

levels at high frequency. The capacitor banks can be seen in 4.7 and 4.8.

The DC-link capacitor which can be seen in 4.8a was chosen larger than  $33 \mu F$  to limit the current ripple and to make the load voltage slow enough for future expansion with communication and PI-regulation. Therefore the capacitance was chosen to  $4700 \mu F$ .

The diodes in the system as seen in 4.8b chosen were Schottky diodes with the average forward current of  $12 A$ . Two of these were placed in parallel at the full bridge rectifier to limit the temperature.

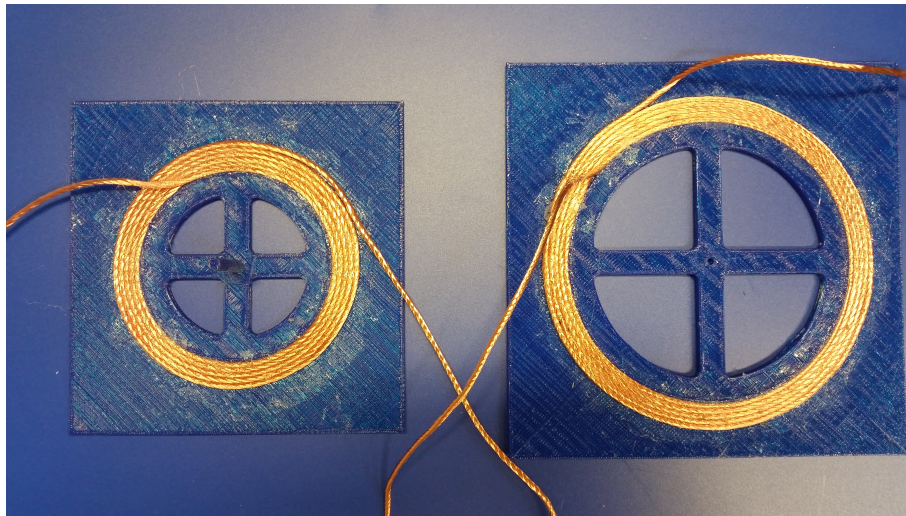


**Figure 4.5:** The two coils used in the IPT. The receiving coil to the left and the transmitting coil to the right, both having 5 turns of litz wire.



(a) Layout of the ferrite plates on the transmitting side.

(b) Layout of the ferrite plates on the receiving side.

**Figure 4.6:** The ferrite arrangement for the coils in 4.5.



#### 4. Design of inductive charging system

---

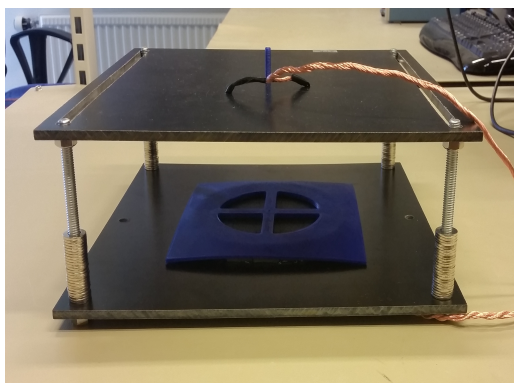
# 5

## Measurement set-up

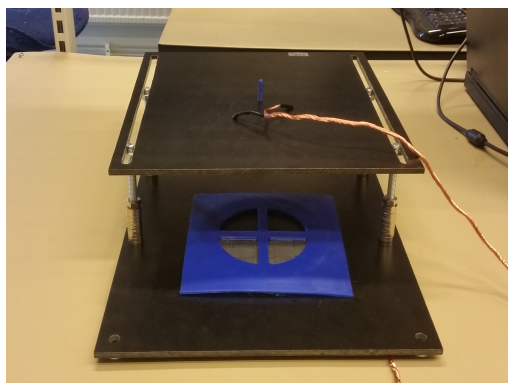
In this chapter the different measurements conducted, measurement equipment and the test stand used are presented.

### 5.1 Lab set-up

To be able to simulate the misalignments the self-balancing robot might do when parking over the power pad a test stand was built as seen in 5.1. The maximum misalignment possible seen from 5.1a to 5.1b is 0 *cm* to 6 *cm*. The power pad also allows changes in air gap from 0 *cm* to 12 *cm*.



(a) Perfect alignment



(b) Maximum misalignment

**Figure 5.1:** Test stand for the transformer. To be able to make changes in air gap and horizontal misalignment

### 5.2 Experimental determination of parameters

In this section the measured values for the components are presented, how they were measured and with what instrument they were measured with.

#### 5.2.1 Self inductance

The self inductance for each coil was measured with the LCR-meter Wayne kerr when the power pads were in perfect alignment. The measured inductance for the transmitting coil was 11.97  $\mu H$  and for the receiving coil was 8.53  $\mu H$ .

### 5.2.2 Mutual inductance

The mutual inductance is measured by doing the "series aiding, series opposing" measurement. This is done by connecting the coils in series in such a way that the magnetic field is aiding each other, and in that way the total measured inductance,  $L_{T1}$ , can be expressed by

$$L_{T1} = L_1 + L_2 + 2M \quad [H] \quad (5.1)$$

The receiving coil is then switched so that the magnetic field is opposing each other, the total inductance,  $L_{T2}$ , is then described by

$$L_{T2} = L_1 + L_2 - 2M \quad [H] \quad (5.2)$$

the mutual inductance is calculated by subtracting (5.1) with (5.2) [21]. These equations form the equation for the mutual inductance as

$$M = \frac{L_{T1} - L_{T2}}{4} \quad [H] \quad (5.3)$$

The total measured inductance,  $L_{T1}$  and  $L_{T2}$ , was then  $27.2 \mu H$  and  $14.9 \mu H$  which gave the mutual inductance of  $3.075 \mu H$ . The measurements was performed with the Wayne kerr LCR-meter at  $100 kHz$ .

### 5.2.3 Capacitance of capacitors

The capacitance was measured with the LCR-meter Wayne kerr. The transmitting resonance capacitor was measured to  $293 nF$  at  $100 kHz$  and for the receiving resonance capacitor it was measured to  $409 nF$  at  $100 kHz$ . The DC-link capacitor was measured to  $4700 \mu F$  at  $10 kHz$ .

## 5.3 Voltage, current and magnetic field measurements

The transmitting side voltage and current was measured with an TEKP5050 voltage probe and P6303 current probe. The current probe measurements was amplified with an AM 503 current probe amplifier. The probes were connected to a Tektronix TDS5034B oscilloscope.

The receiving side voltage and current was measured with an Keysigt N2862B voltage probe and 80i-110s AC/DC current probe. The probes were connected to a Agilent Technologies DSO-X 3014A oscilloscope.

The magnetic field measurements was conducted with a  $6 cm$  loop probe from the Near-field probe set model 7405. The probe was connected to a Tektronix TDS5034B oscilloscope.

# 6

## Results and analysis

In this chapter the results from the performed measurements and simulations are presented, compared and analysed. All the simulations and measurements in this chapter are performed with a load of  $1.15 \Omega$  and  $56 \mu H$ . A switching frequency of  $83 kHz$  is used for the all the simulations and measurements in this chapter and is motivated in section 6.3.1.

Furthermore, unless specified, all simulations and measurements are performed with a duty cycle of 50 % (including the the blanking time). The losses in the inverter are not accounted for and not presented in this chapter. The reason for this is because these losses are relative small and that the inverter has not been designed and built in this project.

### 6.1 Comparison between measured and simulated inductance

The inductance values obtained from the simulations and the measurements can be seen in Table 6.1. The volume and the area of the ferrite pads matches the volume and area used in the simulations. However, the shapes of the ferrite pads does not match the circular shape from the simulations as can be seen in figure 4.6. This is likely the reason for the difference in self-inductance. Furthermore, the shapes of transmitting and receiving power pads do not match each other, which is probably the reason for the lower mutual inductance in the measurements, as the shared area between the coils decreases.

**Table 6.1:** Inductance values obtained from measurements and simulations, as well as difference in percentage compared to the values of the simulations.

	Measurement	COMSOL	Difference
Parameter	With ferrite	With ferrite	[%]
$L_1 [\mu H]$	11.97	12.43	-3.7
$L_2 [\mu H]$	8.53	8.31	+2.6
$M [\mu H]$	3.08	3.78	-18.5

## 6.2 Wave shapes

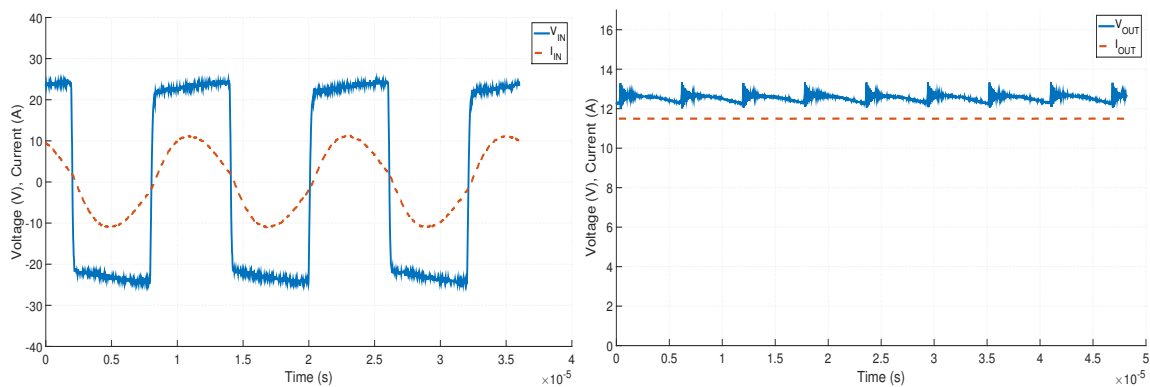
In 6.1a and 6.2a the phase voltage and the phase current of the inverter are presented, henceforth input voltage and input current. In 6.1b and 6.2b the rectified DC-voltage and DC-current is presented, henceforth output voltage and output current.

In 6.1a and 6.2a it can be seen that the voltage and current approximately changes polarity at the same time, indicating good resonance. To note is that the voltage rises and decreases slightly when it reaches the DC value. One explanation of this could be the inductance from the wires between the inverter card and the transmitting resonance card.

This can be seen by comparing 6.2a with 6.3, where the cables are extra long to increase the inductance and enhance the effect of the rise and decrease in the voltage. The inductance for the long and for the shorter cable is measured to  $0.3 \mu H$  and  $0.2 \mu H$ , respectively, for  $100 kHz$ . The induced voltage rise is then calculated to  $2.25 V$  and  $1 V$  during the time interval. When measuring the rise in 6.3 and 6.2a it is measured to approximately  $3.6 V$  and  $1.6 V$ . The remaining difference could depend on stray inductance that has not been accounted for in the IPT system together with the inverter.

The DC supply voltage was tested during operation to see if the DC voltage contained any irregularities during the switching of the MOSFETs, which it did not, excluding it as a source for this problem.

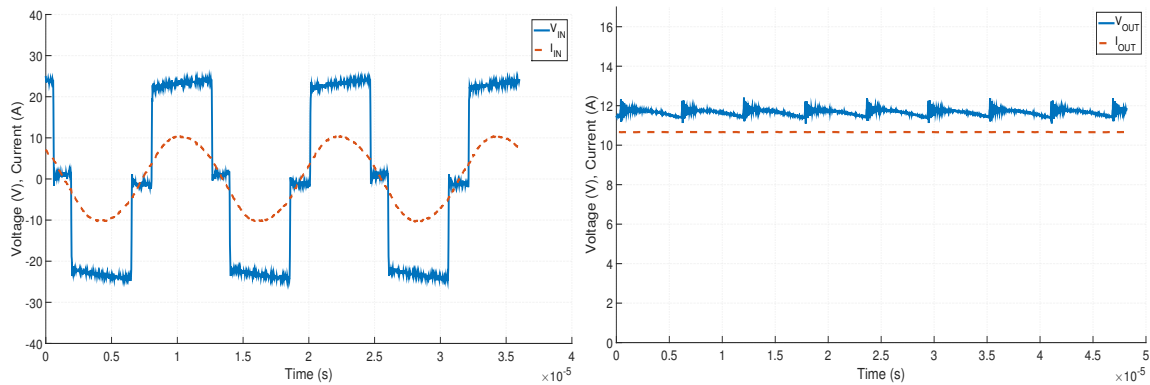
The output voltage ripples with an  $166 kHz$  frequency, due to the full bridge inverter rectifying the  $83 kHz$  signal. The output current has no ripple and this is due to that the load used for the measurements is built as a coil which dampens high frequency currents.



(a) Input voltage and current.

(b) Output voltage and current.

**Figure 6.1:** The measured input and output voltage and current for 50 % duty cycle.



(a) Input voltage and current.

(b) Output voltage and current.

**Figure 6.2:** The measured input and output voltage and current for 40 % duty cycle.

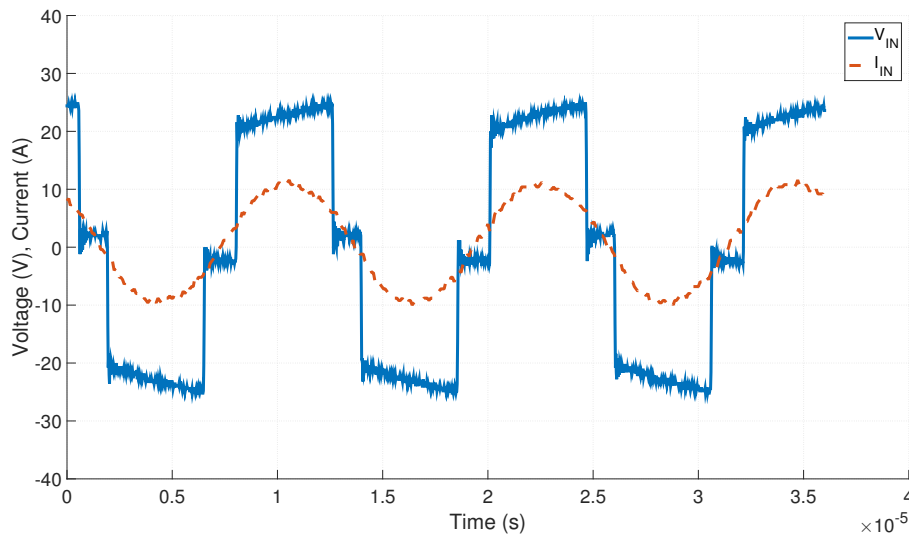


**Figure 6.3:** The measured input voltage and current for 40 % duty cycle, when using extra long cables from the inverter to the IPT.

### 6.2.1 Switching waveforms of MOSFET

In 6.4 the gate-source voltage,  $V_{GS}$ , and the gate-neutral potential,  $V_{GN}$  (seen in 4.3), of two different MOSFETs on the same leg, can be seen. The blanking time between two switching states is lowered to get as fast switching as possible without short-circuiting the inverter. The blanking time is set to approximately 200 ns, which can be seen in 6.5.

This allows the inverter to go to a duty cycle of approximately 4 %. A duty cycle lower than 4 % gives a triangular wave shaped voltage input because the gate-source voltage does not have time to rise enough. Below 2.9 % duty cycle the voltage input becomes 0 V, because the gate-source voltage does not rise above its threshold value.

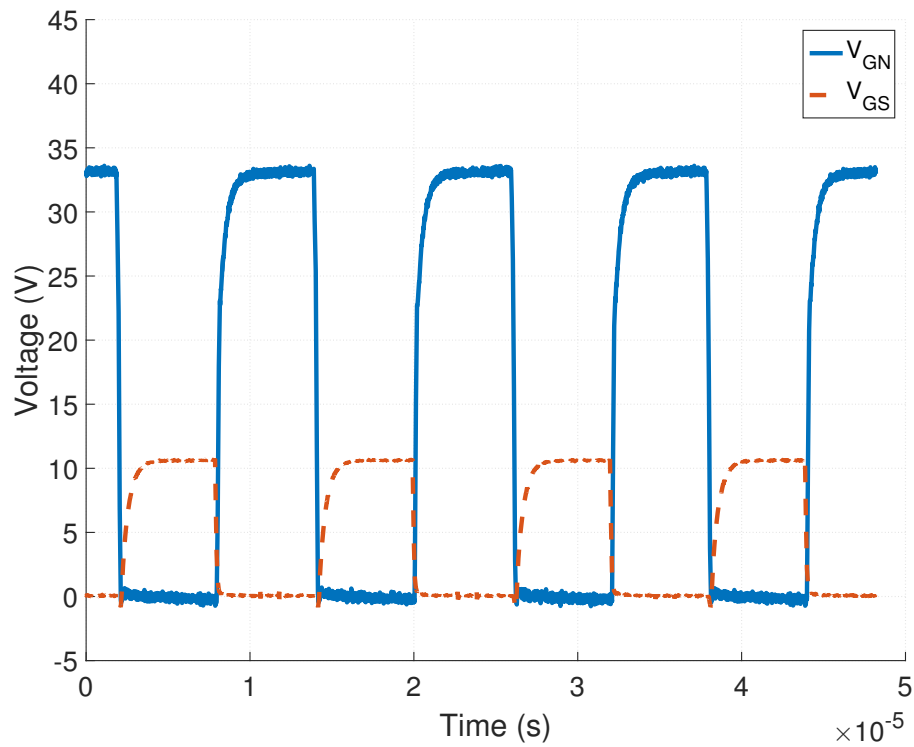
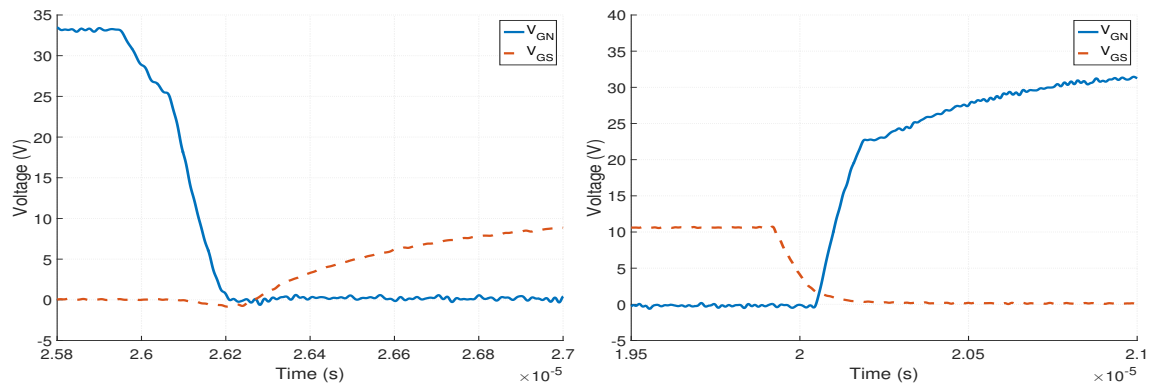


**Figure 6.4:** Gate-source voltage ( $V_{GS}$ ) and potential ( $V_{GG}$ ) of two MOSFETs on the same leg.



(a) Fall time for  $V_{GG}$  and rise time for  $V_{GS}$ , (b) Fall time for  $V_{GS}$  and rise time for  $V_{GG}$ , zoomed.

**Figure 6.5:** Gate-source voltage ( $V_{GS}$ ) and potential ( $V_{GG}$ ) zoomed in for the rise and fall for the two MOSFETs.

### 6.3 Comparison between simulations and measurement

In this section the results from measurements and simulations are analysed and compared.

### 6.3.1 Frequency behaviour

In 6.6a the simulated power/frequency behaviour of the circuit is plotted. From this figure the bi-furcation phenomenon is visible between 60 - 120  $kHz$ . The simulation also shows another bi-furcation point between 20-40  $kHz$ .

In 6.6b the measured power/frequency behaviour of the built circuit is plotted. From this figure the optimal operating point would be around 84  $kHz$  according to the theory in section 2.1.4. At the efficiency plot in 6.7, there is a higher efficiency for 83  $kHz$  than 84  $kHz$  and the power output meet the requirements from the case set-up. Therefore 83  $kHz$  were chosen as the operating frequency.

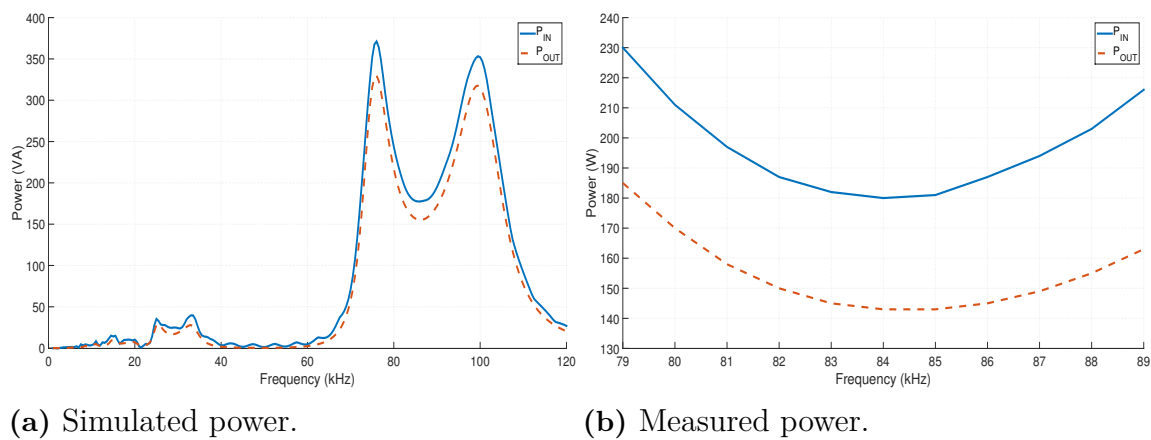


**Figure 6.6:** Simulated and measured input and output active power for different frequencies, with a duty cycle of 50 %.

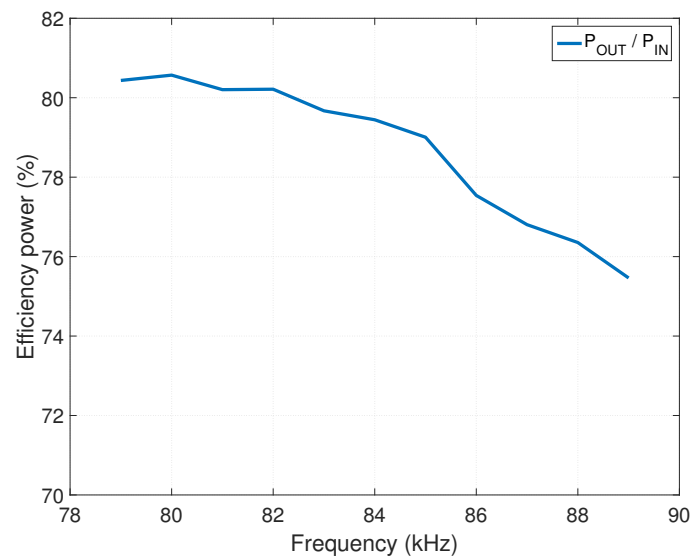


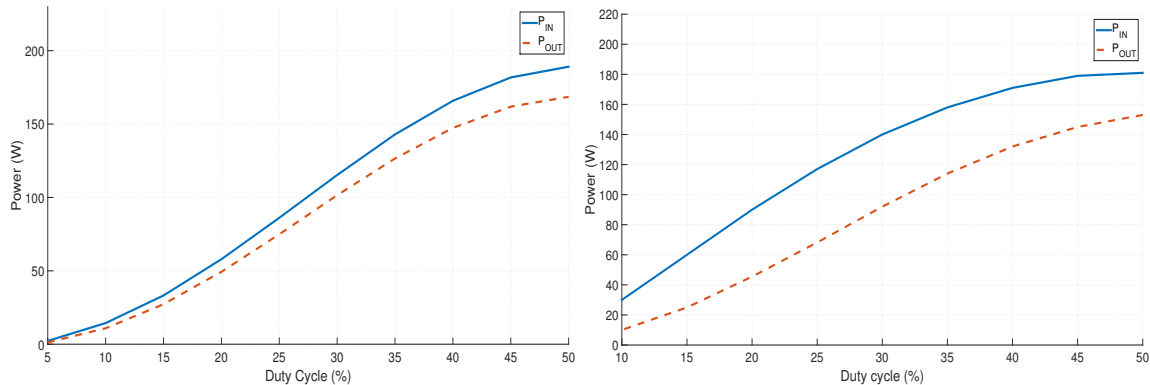
**Figure 6.7:** The measured efficiency of the IPT system for different frequencies.

### 6.3.2 Power transfer and efficiency

In 6.8 and 6.9 the simulated and measured power and efficiency is plotted for different duty cycles. With a 50 % duty cycle the simulated output power is 169 W with an efficiency of 89.1 % and the measured output power is 153 W with an efficiency of 84.5 %.

Some of the difference in power output can be explained by the losses in the ferrite. In 6.10 the total losses for the measured power input and output can be seen. The difference is the highest around 25 % duty cycle. One reason for this is because of the increasing harmonic content of the square-wave voltage with decreasing duty cycle. The THD for the 50 % duty cycle wave is about 45 % and for the 25 % duty cycle wave its about 65 %.

This explains why there is a maximum of losses around 25 % duty cycle, since the eddy currents and the hysteresis losses in the ferrite depends on the frequency and magnetic flux density. It also explains why there is a difference between the simulated result and measured result, since the simulation does not account for the magnetic losses. Furthermore, the losses decreases at lower duty cycles than 25 %, the reason for this is that lower duty cycles results in lower current and thus lower magnetic field density.



(a) Simulated power.

(b) Measured power.

**Figure 6.8:** Simulated and measured input and output active power for different duty cycles.

### 6.3.3 Losses in system

The losses in the system is calculated for 50 % duty cycle which is the maximum efficiency operating point. The losses in the diode bridge rectifier was calculated according to (2.23). The average current and rms current of 5 A and 9.3 A was used, which are taken from the simulations.

The resonance capacitance losses were calculated with the dissipation factor,  $\tan\delta$ , for 100 kHz found in the component data sheet. The DC capacitor losses are

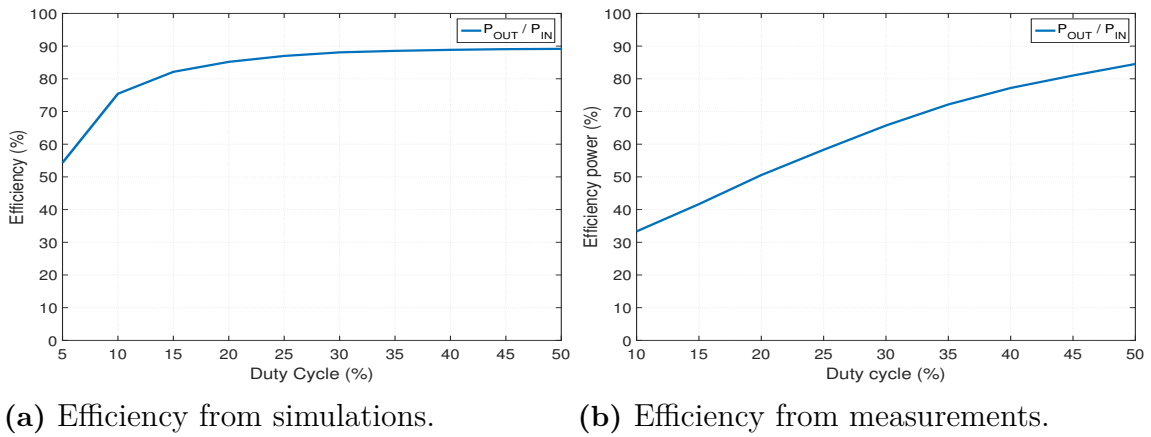


**Figure 6.9:** Simulated and measured efficiency for the active power for different duty cycles.

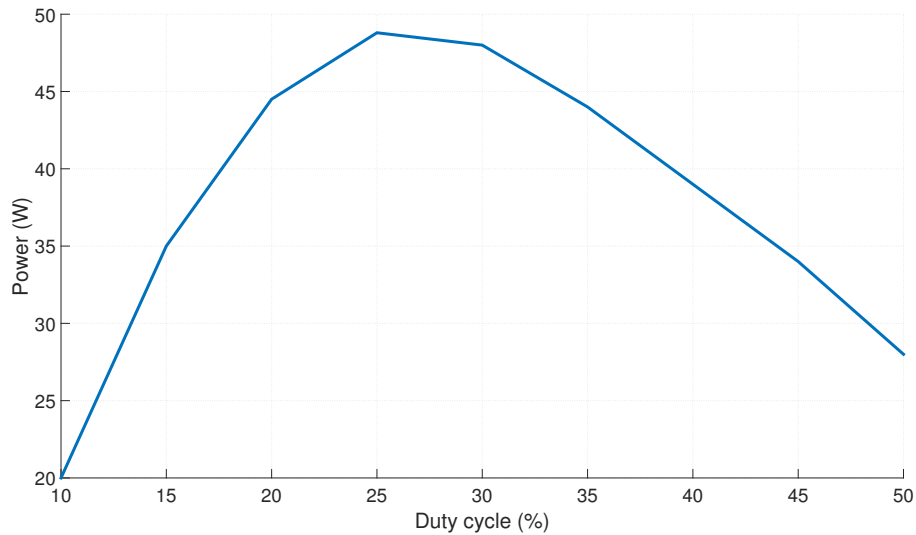


**Figure 6.10:** The losses for the measured system for different duty cycles.

calculated with the equivalent series resistance found in the component datasheet and for the rms current of  $5.7\text{ A}$  from the simulations.

The measured rms currents of the transmitting and receiving coils for 50 % duty cycle is  $7.8\text{ A}$  and  $13.3\text{ A}$ . A resistance measurement was conducted on a non isolated stranded copper wire with the same length as the litz wire on the transmitting and receiving pad. The AC resistance at  $100\text{ kHz}$  was measured to  $1.8\ \Omega$  and to  $1.2\ \Omega$ , compared to the litz-wire resistance of  $0.017\ \Omega$  and  $0.0119\ \Omega$ . Without the litz wire the losses would have been about  $110\text{ W}$  in the transmitting coil and  $210\text{ W}$  in the receiving coil for the measured currents above. Without the litz wire the system would not have been efficient.

The calculated losses for each component can be seen in Table 6.2 and equals  $25.2\text{ W}$ . The total losses for the system at 50 % duty cycle is  $28\text{ W}$ . This means that  $2.8\text{ W}$  is not accounted for.

The losses that are not accounted for are the losses in the ferrite consisting of eddy currents and hysteresis losses and the reverse recovery losses of the diodes. These losses are assumed to be the unknown losses in Table 6.2.

About 73 % of the losses in the system is in the diode bridge rectifier which is to be expected since it is not an efficient method of rectifying, compared to active rectifying.

**Table 6.2:** Calculated losses in the system for 50 % duty cycle.

Component	Power [W]	[%]
Transmitting coil	1	3.6
Receiving coil	1.9	6.8
Primary capacitance bank	0.5	1.8
Secondary capacitance bank	1	3.6
DC capacitor	0.3	1
Diode bridge	20.5	73.2
Other	2.8	10
Total	28	100

## 6.4 Misalignment and change in air gap

The measurements on the misalignment and change in air gap was conducted in such a way that the power output was kept constant at 100  $W$ . This was to simulate the capability of the IPT system to transfer the rated power of the charger.

### 6.4.1 Misalignment between power pads

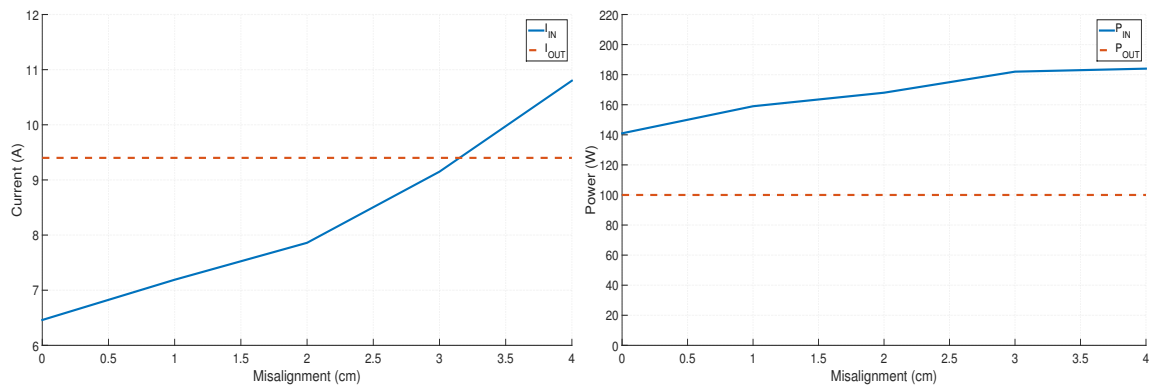
In 6.11 the input and output current and power can be seen. For an increasing misalignment the input current increases to be able to supply the load with 100  $W$ . This since the leakage flux increases and the mutual flux decreases with increasing misalignment. The efficiency of the IPT system is seen in 6.12 and decreases from 71 % to 54 % for 100  $W$  power transfer.

### 6.4.2 Change in air gap

In 6.13 the input and output current and power can be seen. At 2  $cm$  air gap the system was not able to transfer 100  $W$ , because the impedance of the system becomes too high with the increasing self-inductance's.

The same behaviour as in the misalignment case can be seen for the changes in air gap, with increasing current for increasing air gap, to be able to transfer 100  $W$ .

In 6.14 the efficiency can be seen. The efficiency decreases from 77 % to 58 % in the IPT system when transferring 100  $W$ .



(a) The measured rms current.

(b) The measured power.

**Figure 6.11:** Input and output current and power for different misalignment in  $cm$ .

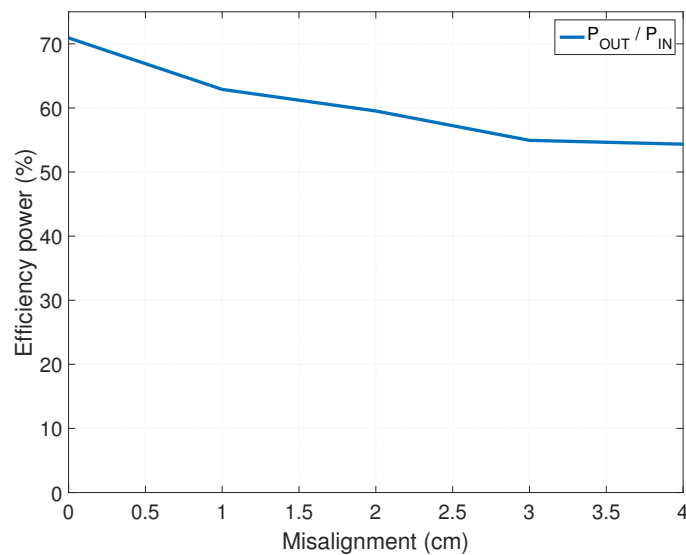


**Figure 6.12:** The efficiency of the IPT system for different misalignment, when transferring 100  $w$ .

## 6.5 Heat dissipation

In 6.15 - 6.17 the heat dissipation of the components are presented. As seen in 6.15b the diode bridge rectifier has the highest temperature, 130  $^{\circ}C$ . The the diodes are rated for temperatures up to 150  $^{\circ}C$ .

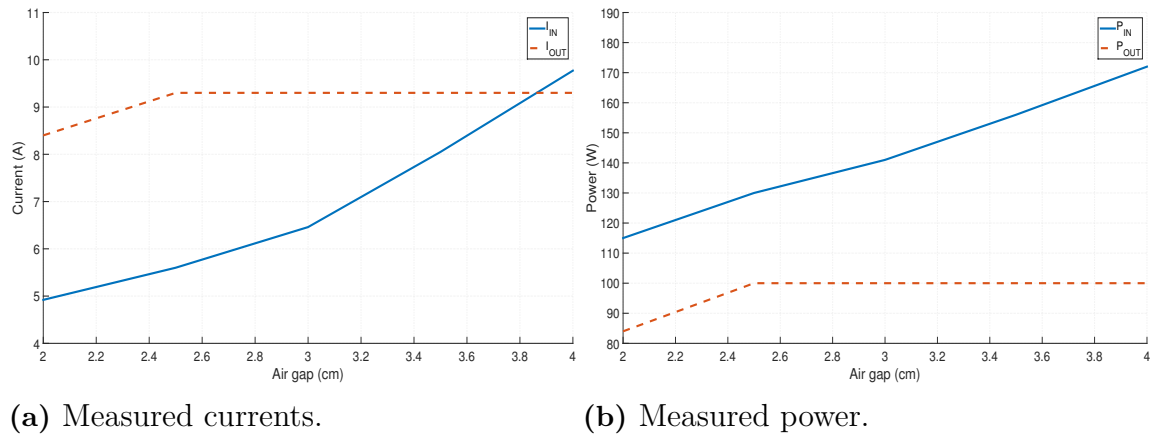


**Figure 6.13:** Input and output currents and power, for different air gaps in *cm*.

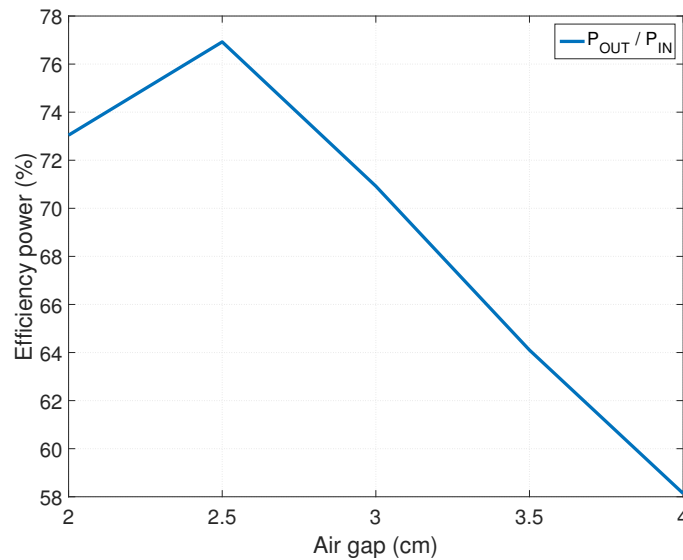


**Figure 6.14:** The efficiency of the IPT system for different air gaps, when transferring 100 W.

## 6.6 Magnetic field

The magnetic field density is measured above the receiving charging pad and can be seen in 6.18a. The maximum magnetic flux density is measured closest to the power pad to 0.2 *mT*. It can be seen that the magnetic flux density has decreased significantly 7 *cm* away from the power pad. Between the two coils the magnetic field density is strongest at the receiving pad, where it is approximately 2 *mT*. The reason for this is that the receiving coil has a higher RMS current.

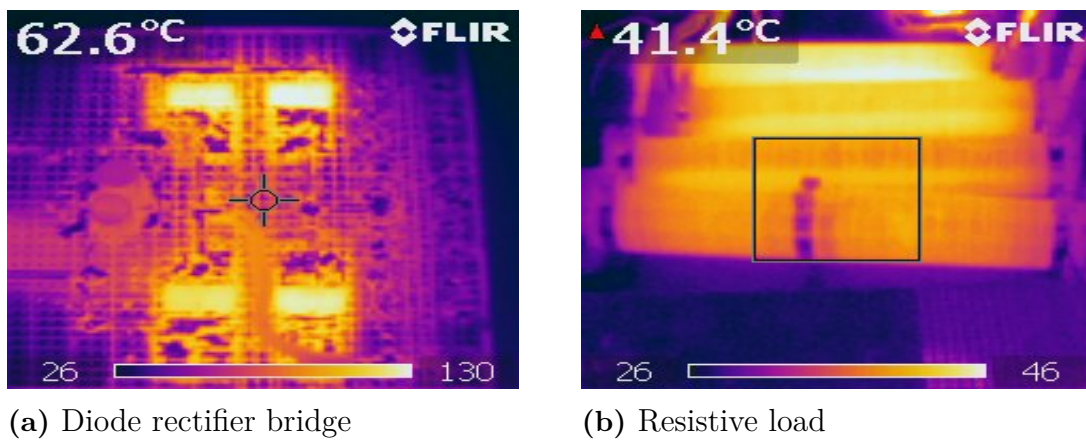


**Figure 6.15:** Heat dissipation of the diode bridge and the load.

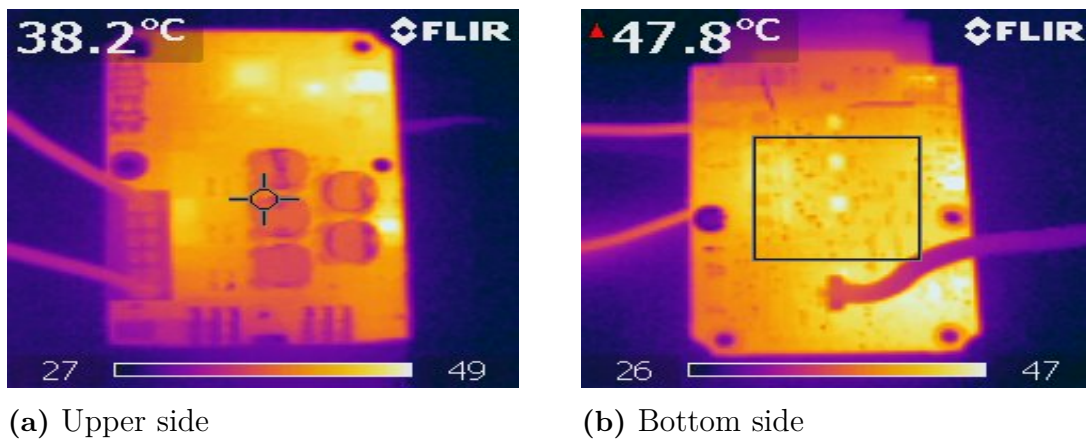


**Figure 6.16:** Heat dissipation of the circuit board with the full bridge inverter

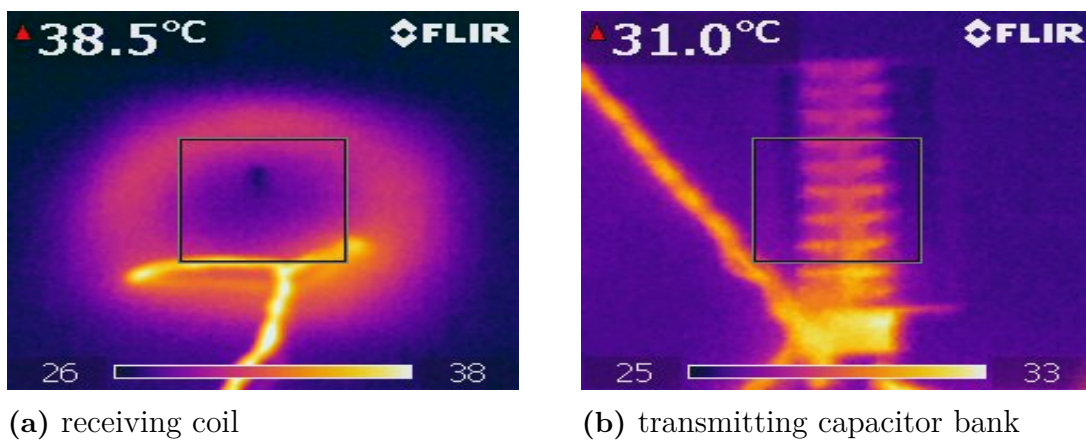
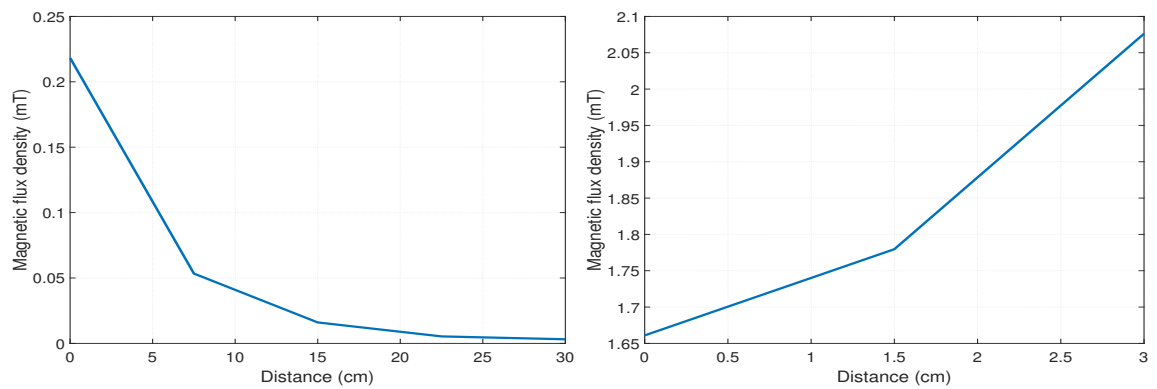


**Figure 6.17:** Heat dissipation of the receiving coil and the transmitting capacitor bank bridge and the load.



(a) Magnetic flux density above receiving coil. (b) Magnetic flux density between coils, from sending to receiving.

**Figure 6.18:** The rms value of the magnetic flux density at different positions.

# 7

## Conclusions

The aim of transferring 150  $W$  for a 3  $cm$  air gap with an efficiency over 80 % is achieved. The IPT system can transfer 153  $W$  with an efficiency of 84.5 %. Furthermore, the IPT system is able to fully charge the lithium-ion batteries of the robot via a charger with a battery management system, autonomous and wireless. Also, the IPT system is able to transfer 100  $W$ , which is the maximum input power of the charger, with a misalignment of 4  $cm$  as well as an increased air gap to 4  $cm$ .

Most losses occur in the diode bridge rectifier. The losses consist of conduction and reverse recovery losses of the diodes. These losses are high due to high currents and high threshold voltage. The losses and heat dissipation is kept down by using two diodes in parallel, dividing the current. These losses can be decreased by replacing the diode bridge rectifier with an active rectification bridge, using MOSFETs instead of diodes, which have a lower conducting resistance.

The losses that occur in the in the receiving coil are larger than the losses in the transmitting coil, depending on higher currents in the receiving coil. These losses are dependent on the on the AC resistance of the wires which are kept down by using litz wires. However, if a solid wire would be used instead the losses would be extremely high, making the litz wire necessary.

The efficiency of the IPT system for lower duty cycles is lower than the the efficiency obtained from the simulations. This most likely depends on the losses in the ferrite, which was not accounted for in the simulations. The eddy current losses in the ferrite is proportional to the square of magnetic flux density and the frequency. The hysteresis losses in the ferrite is proportional to frequency and dependent of the magnetic flux density. As the square-wave voltage for lower duty cycles has more harmonic content this can explain the high losses at around 25 % duty cycle. Furthermore, the losses from the reverse recovery losses in the diodes are not accounted for.

### 7.1 Future work

The performance of the IPT system should be tested with an aluminium casing. This as the self-balancing robot is covered in aluminium and the efficiency of the IPT system may be affected with the casing of the secondary power pad. Furthermore, shielding vertically along the IPT system should be considered. This to make

## 7. Conclusions

---

the systems safe to humans very close by and to decrease the electromagnetic/radio-frequency interference with the circuits on the robot.

To decrease the losses in the ferrite one could increase the cross-sectional area of the ferrite material close to the litz wire. This to decrease the magnetic flux density and thus the losses.

Furthermore, and probably the most important improvement is to replace the diode bridge rectifier with an active rectification bridge. In the diode bridge rectifier, most losses occur and to decrease these losses it would have a significant effect on the efficiency of the IPT system.

The IPT system should in the future be implemented in the robot. However, if the system should use the currently used charger, one must manually boot the charger. This may cause some trouble design-wise as the charger has to be reachable and can thus not be inside of the robot as well as the inconvenience of reaching down to manually boot it. Furthermore, the size of this charger will also cause some problems as it is relative large and there are two battery packages in the robot, requiring two charging occasions.

One solution to this problem is to create a separately battery management system and charge the batteries directly without a charger. If 24 V should be applied directly on the batteries, the windings of the coils needs to be re-winded, to be able to transfer desired power. This will need some modifications in the capacitor banks as the values of the inductance will change. Furthermore, a new control algorithm is thus needed as when directly charging the lithium-ions batteries constant voltage constant current control is needed.

Furthermore, a properly 3D-print design for the litz wire and the ferrite plates could be useful when implementing the system in the robot. In this way the size can be kept down and it would make the system reliable and robust. This 3D-design could also give room for shielding on the vertically sides of the system if needed.

Also, the lab-card on the transmitting and receiving side could be rebuild on a PCB-board. In this way size could be decreased and fan cooling could be implemented as well.

# Bibliography

- [1] Proxi. (2016, May 3) Wireless Charging [Online]. Available: <http://powerbyproxi.com/wireless-charging/>.
- [2] G. Ombach et al., "Optimum magnetic solution for interoperable system for stationary wireless EV charging", in Tenth International Conference on Ecological Vehicles and Renewable Energies., München, Conf. 2015.
- [3] R. Walli. (2016), *ORNL surges forward with 20-kilowatt wireless charging for vehicles* [online], available FTP: <https://www.ornl.gov/news/ornl-surges-forward-20-kilowatt-wireless-charging-vehicles>.
- [4] S. Chopra and P. Bauer, "Analysis and Design considerations for a Contactless Power Transfer System", Delft University of Technology, Netherlands, Rep. 978-1-4577-1250-0, 2011.
- [5] P. Mattsson and K. Olsson, "High efficiency inductive charging for electric mini-cars", Chalmers University of Technology, Dept. of Energy and Environment, 2015.
- [6] D.K. Cheng, "Static Magnetic Fields" in *Field and Wave Electromagnetics*, 2nd ed., ADDISON WESLEY publishing company, pp. 233-239.
- [7] S. Moon et al., "Analysis and Design of Wireless Power Transfer System with an Intermediate Coil for High Efficiency", Dept. of Elect. Eng., Kaist, Rep. 978-1-4799-0482-2, 2013.
- [8] H. A. Ghali, "Understand Mutual Inductance" using COMSOL Multiphysics" *COMSOL Conference 2009 Milan*, Milan, 2009.
- [9] S. Moon et al., "Analysis and Design of Wireless Power Transfer System with an Intermediate Coil for High Efficiency", Dept. of Elect. Eng., Kaist, Rep. 978-1-4799-0482-2, 2013.
- [10] Wireless Power Consortium, *Magnetic Resonance and Magnetic Induction - What is the best choice for my application?* [online], available FTP: <https://www.wirelesspowerconsortium.com/data/downloadables/1/2/4/6/magnetic-resonance-or-magnetic-induction.pdf>.

- [11] S. Chopra and P. Bauer, "Analysis and Design considerations for a Contactless Power Transfer System", Delft University of Technology, Netherlands, Rep. 978-1-4577-1250-0, 2011.
- [12] S. Moon et al., "Analysis and Design of Wireless Power Transfer System with an Intermediate Coil for High Efficiency", Dept. of Elect. Eng., Kaist, Rep. 978-1-4799-0482-2, 2013.
- [13] N.M et al., "SWITCH-MODE dc-ac INVERTERS: dc  $\leftrightarrow$  SINUSOIDAL ac" in *Power Electronics CONVERTERS, APPLICATIONS AND DESIGN*, 3rd ed., John Wiley & Sons, pp. 218.
- [14] A. Namboodiri and H. S. Wani, "Unipolar and Bipolar PWM Inverter", Dept. Power Elect. Eng, Vishwakarma Govt. Eng. Collage, Chandkeda, Rep. 2349-6010, 2014.
- [15] N.M et al., "POWER MOSFETs" in *Power Electronics CONVERTERS, APPLICATIONS AND DESIGN*, 3rd ed., John Wiley & Sons, pp. 584-587.
- [16] *Power MOSFET Basics*, Alpha & Omega SEMICONDUCTOR, North America, CA.
- [17] N.M et al., "Single-phase diode bridge rectifiers" in *Power Electronics CONVERTERS, APPLICATIONS AND DESIGN*, 3rd ed., John Wiley & Sons, pp. 86.
- [18] K.A Kuhn, "Power supplies - - Filter capacitor", July 26, 2006.
- [19] *Calculation of power losses*, 3rd ed., Applicat., STMicroelectronics, Geneva Switzerland, August 2011, pp. 3-5.
- [20] H. A. Ghali, "Understand Mutual Inductance" using COMSOL Multiphysics" *COMSOL Conference 2009 Milan*, Milan, 2009.
- [21] *Agilent Impedance Measurement Handbook*, 4th edition, Agilent Technologies, pp. 5-14.